Publications of the Astronomical Society of Australia (PASA), Vol. 30, e038, 23 pages.

doi:10.1017/pasa.2013.18

Characterisation of the MALT90 Survey and the Mopra Telescope at 90 GHz

J. B. Foster[1,2,18], J. M. Rathborne[3], P. Sanhueza[2], C. Claysmith[2], J. S. Whitaker[4], J. M. Jackson[2], J. L. Mascoop[2], M. Wienen[5], S. L. Breen[3], F. Herpin[6,7], A. Duarte-Cabral[6,7], T. Csengeri[5], Y. Contreras[3], B. Indermuehle[3], P. J. Barnes[8], A. J. Walsh[9], M. R. Cunningham[10], T. R. Britton[3,11], M. A. Voronkov[3], J. S. Urquhart[5], J. Alves[12], C. H. Jordan[3,13], T. Hill[14,15], S. Hoq[2], K. J. Brooks[3] and S. N. Longmore[16,17]

[1]Yale Center for Astronomy and Astrophysics, Yale University, New Haven, CT 06520, USA
[2]Institute for Astrophysical Research, Boston University, Boston, MA 02215, USA
[3]CSIRO Astronomy and Space Science, PO Box 76, Epping, NSW 1710, Australia
[4]Physics Department, Boston University, Boston, MA 02215, USA
[5]Max-Planck-Institut für Radioastronomie, Auf dem Hügel 69, D-53121 Bonn, Germany
[6]University of Bordeaux, LAB, UMR 5804, F-33270 Floirac, France
[7]CNRS, LAB, UMR 5804, F-33270 Floirac, France
[8]Astronomy Department, University of Florida, Gainesville, FL 32611, USA
[9]International Centre for Radio Astronomy Research, Curtin University, GPO Box U1987, Perth WA 6845, Australia
[10]School of Physics, University of New South Wales, Sydney, NSW 2052, Australia
[11]Department of Physics and Astronomy, Macquarie University, Sydney, NSW 2109, Australia
[12]Department of Astrophysics, University of Vienna, Türkenschanzstrasse 17, 1180 Vienna, Austria
[13]School of Mathematics and Physics, University of Tasmania, Private Bag 37, Hobart, Tasmania 7001, Australia
[14]Laboratoire AIM Paris-Saclay, CEA/IRFU-CNRS/INSU-Université Paris Diderot, CEA Saclay, 91191 Gif-sur-Yvette Cedex, France
[15]Joint ALMA Observatory, Alonso de Córdova 3107, Vitacura 763-0355, Santiago, Chile
[16]Astrophysics Research Institute, Liverpool John Moores University, Twelve Quays House, Egerton Wharf, Birkenhead CH41 1LD, UK
[17]European Southern Observatory, Karl-Schwarzschild-Strasse. 2, D-85748 Garching bei München, Germany
[18]Email: jonathan.b.foster@yale.edu

(Received May 21, 2013; Accepted June 2, 2013; Online Publication July 10, 2013)

Abstract

We characterise the Millimetre Astronomy Legacy Team 90 GHz Survey (MALT90) and the Mopra telescope at 90 GHz. We combine repeated position-switched observations of the source G300.968+01.145 with a map of the same source in order to estimate the pointing reliability of the position-switched observations and, by extension, the MALT90 survey; we estimate our pointing uncertainty to be 8 arcsec. We model the two strongest sources of systematic gain variability as functions of elevation and time-of-day and quantify the remaining absolute flux uncertainty. Corrections based on these two variables reduce the scatter in repeated observations from 12%–25% down to 10%–17%. We find no evidence for intrinsic source variability in G300.968+01.145. For certain applications, the corrections described herein will be integral for improving the absolute flux calibration of MALT90 maps and other observations using the Mopra telescope at 90 GHz.

Keywords: astrochemistry – H II regions – instrumentation: spectrographs – ISM: individual (RCW 65) – radio lines: ISM – telescopes

1 INTRODUCTION

The Millimetre Astronomy Legacy Team 90 GHz Survey (MALT90) is characterising the physical and chemical conditions of dense molecular clumps associated with high-mass star formation over a wide range of evolutionary states using the ATNF (Australia Telescope National Facility) Mopra 22-m radiotelescope (J. M. Jackson et al., in preparation). MALT90 targets are chosen from the APEX (Atacama Pathfinder Experiment) Telescope Large Area Survey of the Galaxy (ATLASGAL; Schuller et al. 2009; Contreras et al. 2013). This paper presents an analysis of G300.968+01.145 (G301), and uses our repeated position-switched (PSW) observations of this source to characterise the system performance of the Mopra telescope as used in the MALT90 survey, including the pointing reliability, systematic gain variation, and the absolute flux uncertainty.

Our primary goal in observing G301 was to ascertain good system performance at the start of each observing session. G301 was chosen based on its Galactic position and its

relative brightness in many transitions in the MALT90 pilot survey (Foster et al. 2011). A typical observing session commenced with a pointing on an SiO maser, followed by a PSW observation of G301 and a quick examination of the resulting spectrum. If the transitions of G301 were detected at the expected level, it demonstrated that the system was working well, and the rest of the observations continued.

Although this system check was the main purpose of the PSW observations of G301, our repeated observations of the same source under different conditions allow us to carry out a detailed assessment of the systematics and error budget of our survey, as well as to characterise aspects of the performance of the Mopra telescope at 90 GHz. The beam size, beam shape, and efficiency of the Mopra telescope have previously been measured at 90 GHz and 16–50 GHz (Ladd et al. 2005; Urquhart et al. 2010), and this paper focuses on characterising other aspects of the Mopra telescope at 90 GHz.

G301 is a molecular clump associated with the ultracompact H II region (UC H II region), known as RCW 65 (Rodgers, Campbell, & Whiteoak 1960) or Gum 43 (Gum 1955). G301 contains prominent OH masers at 1 665 and 1 667 MHz; it has been studied extensively over the past 40 years (e.g. Robinson, Caswell, & Goss 1974) and has been found to contain numerous other maser features, including OH masers at 6 035 and 6 030 MHz (Caswell, Kramer, & Reynolds 2009) and a methanol maser at 6 668 MHz (Caswell 1997). On the basis of the maser data, Caswell et al. (2009) conclude that this source is a canonical example of an OH maser in a high-mass star-forming region, with a cluster of maser spots projected against a UC H II region; they regard the source as near the end of the evolutionary period in which it is capable of supporting maser emission, suggesting an age for the UC H II region near the lifetime of such objects, $\sim 10^5$ years (Churchwell 1999).

As a well-known southern high-mass star-forming region, G301 has been included in a large number of studies, including searches for other masers (e.g. Caswell 2003; Dodson & Ellingsen 2002), studies measuring the magnetic fields in H II regions (e.g. Han & Zhang 2007), continuum surveys of southern regions of high-mass star formation (e.g. Faúndez et al. 2004; Walsh et al. 1998, 1999, 2001; Kwok, Volk, & Bidelman 1997), and observations of dense gas tracers such as NH_3 (1, 1) (Vilas-Boas & Abraham 2000), $C^{18}O$ (2 − 1) and HNCO ($10_{0,10}$– $9_{0,9}$) (Zinchenko et al. 2000), and isotopologues of CS (Chin et al. 1996). The 6-GHz Methanol Multibeam (MMB) survey used G301 to check their calibration stability (Green et al. 2009).

UC H II regions have variable continuum emission on the timescale of years (e.g. Franco-Hernández & Rodríguez 2004; Galván-Madrid et al. 2008). It is possible, therefore, that the molecular line emission from a UC H II region such as G301 could also be variable on these timescales. Typical timescales for significant changes in molecular abundances due to chemistry are $>10^3$ years (e.g. van Dishoeck & Blake 1998; Viti et al. 2004) although some chemistry in 'hot cores' around massive protostars may take place on timescales of $10^{2.5}$ years (Chapman et al. 2009). This is still long compared with the timescale for continuum variability.

In the simulations of Peters et al. (2010) and Galván-Madrid et al. (2011), the continuum variability in a UC H II region arises from the shielding of the ionising source by its own accretion flow. They note that since the mass of ionised gas is typically much less than the mass of molecular gas observed in a UC H II region, the variability of the molecular gas due to small clumps of mass becoming ionised or recombining would be much less than the continuum variability. Another model which explains H II region variability via variations in the ionising source itself (Klassen, Peters, & Pudritz 2012) does not produce sufficiently large continuum emission variability on the appropriate timescales to account for the observations of Franco-Hernández & Rodríguez (2004) and Galván-Madrid et al. (2008). In the Klassen et al. (2012) model, molecular line emission should vary only on timescales of thousands of years. Therefore, we consider it highly unlikely that the molecular line emission from G301 will be intrinsically variable, although we briefly consider this possibility.

2 OBSERVATIONS

2.1 Position-switched observations

We typically observed G301 once at the beginning of each observing session. Throughout this paper, we shall refer to a single block of observing time as a 'session' or an 'observing session' (sessions were typically 11–14 h in duration) and we shall use the term 'season' or 'observing season' to refer to the time period during which our observations were conducted during the year. We had three observing seasons from July to September in 2010, from May to October in 2011, and from May to October in 2012. During the first two observing seasons, G301 was typically between 35°–40° of elevation at the start of our observing sessions. During our third observing season, sessions started at a later local sidereal time, so G301 was typically between 55°–60° of elevation at the start of an observing session.

We occasionally obtained additional observations of G301 during a given session or at atypical elevations for a variety of reasons, such as (1) mechanical failure or bad weather delaying the start of an observing session, (2) a non-standard start time for an observing session (due to the schedule of other projects), and (3) in order to better characterise G301 for this analysis. We performed a total of 258 observations of G301. A small number (10) of observing sessions for MALT90 started after G301 had set, in which case system checks were performed on another source (G337.005+00.323), but the sample of observations of G337.005+00.323 is too small to be useful for characterisation and is not considered here.

We obtained a single PSW observation with 150 s of on-source integration time interlaced with an equal amount of time spent on a reference position at +1° in Galactic

latitude. The observing pattern was off–on–on–off–off–on–on–off–off–on with individual integrations of 30 s. Both linear polarisations were observed, and were averaged together for all the following analysis.

A PSW observation of G301 always immediately followed a successful pointing correction routine on an SiO maser (hereafter we refer to this process as 'pointing'). In subsequent observing, we pointed on an SiO maser before every source, roughly once an hour. The pointing precision of PSW observations G301, immediately following a pointing correction, is therefore typical of the pointing precision of our maps. Several different SiO masers were used as the pointing source for PSW observations of G301. During the first observing season, we most commonly used X Cen, and during the second and third observing seasons we most commonly used RW Vel. In addition, we sometimes used IRSV 1540, W Hya, and VX Sgr.[1] Unfortunately, the often strong intrinsic brightness variability of SiO masers and our inconsistent use of a single pointing source precludes us from being able to use the brightness of the pointing source for characterisation.

Immediately following a PSW observation of G301, we returned to perform a pointing correction on an SiO maser (the particular maser varied based on the location of the source to be subsequently observed). The offsets (in azimuth and elevation) deduced from this pointing correction routine were recorded automatically and these offsets can be used as an additional estimate of pointing precision.

We observed G301 using the same frequency setup as for the full survey (J. M. Rathborne et al.,in preparation), with 16 spectral windows of 138 MHz each providing $\sim$0.11 km s^{-1} velocity resolution around 16 rest frequencies corresponding to our targeted transitions. In this paper, we focus on the four strongest transitions, highlighted in bold in Table 1. These are all ground-state ($J = 1 - 0$) transitions, and henceforth we shall refer to these transitions only by the molecule or ion (i.e. N_2H^+ instead of N_2H^+ $J = 1 - 0$).

2.2 Mapping observations

In addition to the PSW observations, we obtained three 3 $\times$3 arcmin^2 maps of G301. The first map was obtained as part of the regular survey, and subsequent maps were obtained to increase the signal-to-noise ratio of the map and to assist in measuring the pointing and flux uncertainty. These maps were taken in the normal mode for the survey (see J. M. Rathborne et al.,in preparation), with two on-the-fly maps made by scanning both in Galactic latitude and Galactic longitude. We consider only the T_{sys} weighted co-addition of the two different scan maps in this analysis since the pointing error between the two scan maps made in different directions will be minimal. Table 2 displays the UT date and time, as well as the measured T_{sys} and elevation, of the maps of G301.

Table 1. Spectrometer configuration.

IF[a]	Species	Main transition	ν (GHz)[b]
0	**N_2H^+**	$\boldsymbol{J = 1 - 0}$	**93.17377**
1	^{13}CS	$J = 2 - 1$	92.49430
2	H	41α	92.03448
3	CH_3CN	$J_K = 5_1 - 4_1$	90.97902
4	HC_3N	$J = 10 - 9$	91.19980
5	$^{13}C^{34}S$	$J = 2 - 1$	90.92604
6	**HNC**	$\boldsymbol{J = 1 - 0}$	**90.66357**
7	$HC^{13}CCN$	$J = 10 - 9, F = 9 - 8$	90.59306
8	**HCO^+**	$\boldsymbol{J = 1 - 0}$	**89.18853**
9	**HCN**	$\boldsymbol{J = 1 - 0}$	**88.63185**
10	HNCO	$J_{K_a,K_b} = 4_{0,4} - 3_{0,3}$	88.23903
11	HNCO	$J_{K_a,K_b} = 4_{1,3} - 3_{1,2}$	87.92524
12	C_2H	$N = 1 - 0$ $J = \frac{3}{2} - \frac{1}{2}, F = 2 - 1$	87.31692
13	$HN^{13}C$	$J = 1 - 0$	87.09086
14	SiO	$J = 2 - 1$	86.84701
15	$H^{13}CO^+$	$J = 1 - 0$	86.75433

[a]This paper will focus on the four transitions shown in bold in this table.
[b]Uncertainties on rest frequencies are less than the spectral resolution.

Table 2. Maps of G301.

UT Date_Time	Direction	$\langle T_{sys} \rangle$ (K)	$\langle$Elevation$\rangle$ (deg)
2011-05-06_1527	GLat	169.0	41.5
2011-05-06_1558	GLon	173.5	37.8
2011-08-22_0034	GLat	160.5	42.4
2011-08-22_0104	GLon	159.8	46.0
2012-06-29_0657	GLat	184.1	58.6
2012-06-29_0727	GLon	181.0	59.6

3 REDUCTION

Reductions of the PSW observations were carried out in the ASAP[2] package by (1) producing a quotient spectrum from adjacent on and off observations, (2) performing frequency alignment (of minimal importance during such a short series of observations), (3) averaging the two linear polarisations together using T_{sys} weighting, and (4) averaging the five different on–off cycles using T_{sys} weighting. Finally, we fit the baseline within each IF with a second-order polynomial, excluding 300 channels (out of a total of 4 096) at the edge of each IF. Note that this procedure does not include a gain–elevation correction, as this has not been accurately measured for the Mopra telescope at 90 GHz; the derivation of the gain–elevation correction from these data is one of the goals of this paper. Because the Mopra telescope uses a paddle for T_{sys} calibration at 90 GHz, our data are already opacity corrected.

The maps of G301 were reduced using the MALT90 reduction pipeline, which uses the ATNF packages LIVEDATA and GRIDZILLA[3] to produce a map from the on-the-fly data.

[1] See http://www.narrabri.atnf.csiro.au/cgi-bin/ obstools/siomaserdb.cgi for details of these SiO masers.

[2] http://svn.atnf.csiro.au/trac/asap
[3] http://www.atnf.csiro.au/computing/software/livedata/index.html

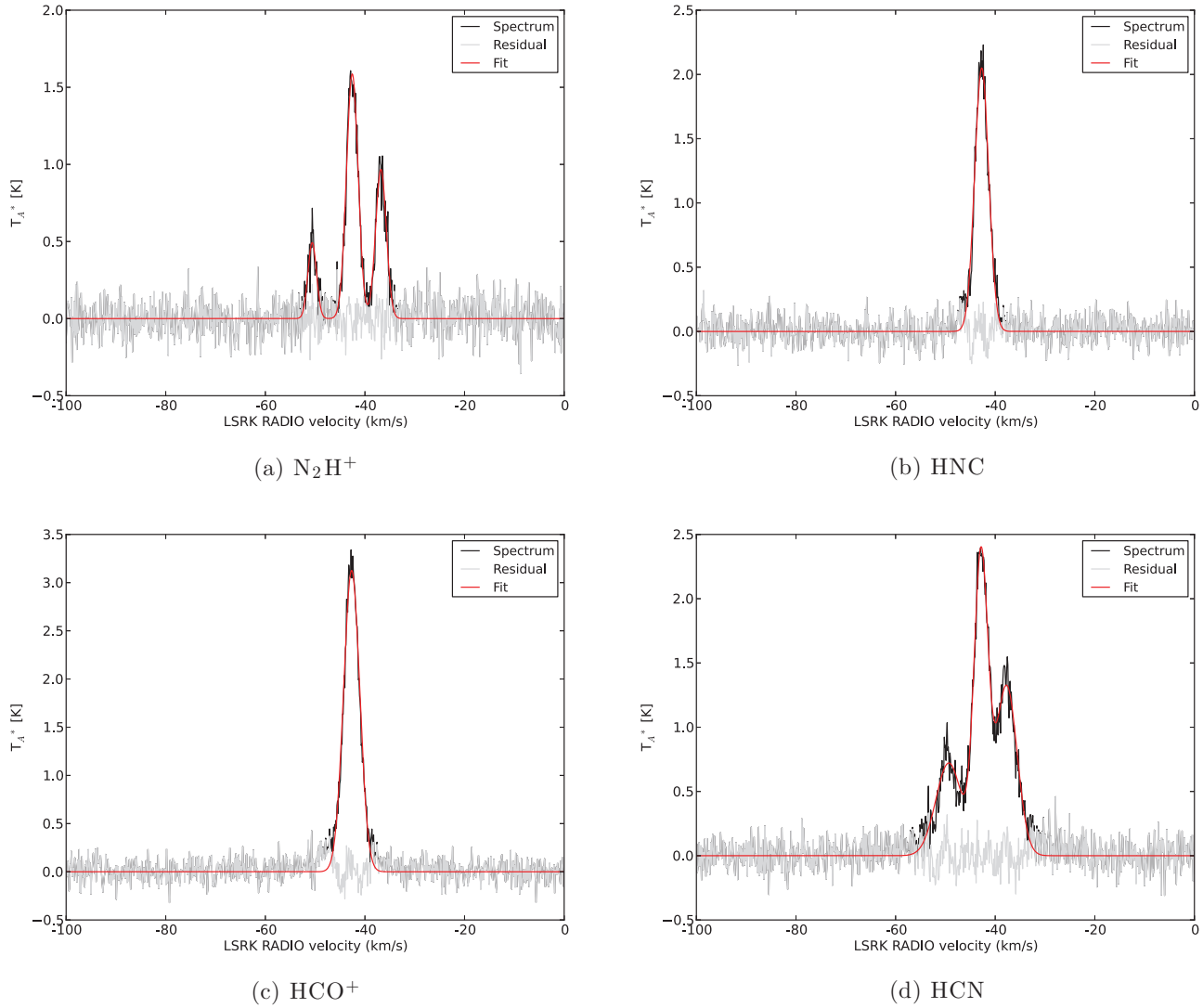

(a) N_2H^+ (b) HNC

(c) HCO^+ (d) HCN

Figure 1. Gaussian fits of the four strongest transitions for a typical PSW spectrum of G301 (2011-09-26_1). The data are in black, the fit is shown in red, and the residual is in grey.

The pipeline performs reference subtraction (with reference positions $\pm 1^\circ$ away from the Galactic plane), polarisation averaging, baseline subtraction with a second-order polynomial fit (excluding 300 channels on the edge of the bandpass out of a total of 4 096 channels) and $T_{\rm sys}$ weighted co-addition of the spectra within the maps to produce a lightly smoothed map with an effective beam of 38 arcsec. Our modified pipeline version of LIVEDATA applies an 11-channel Hanning smoothing kernel to the reference spectra before subtracting them from the source spectra in order to mitigate striping artefacts in the maps.

All data in this paper are presented on the antenna temperature T^*_A scale. The main beam efficiency for the Mopra telescope at 90 GHz was estimated to be 0.49 $\pm$ 0.03 by Ladd et al. (2005). For compact sources (<80 arcsec), division by this number would approximately convert our antenna temperature measurements into main-beam brightness temperatures, although additional efficiency corrections (i.e. gain factors) are derived in this work, which suggests that additional corrections are required.

3.1 Spectral line fitting

Following basic reduction, we fit the four strongest transitions (N_2H^+, HNC, HCO^+, and HCN) with a number of Gaussians corresponding to the number of resolved components present. N_2H^+ and HCN are each fitted with three Gaussians with fixed velocity separations and initial intensity ratios appropriate for the optically thin hyperfine components. HNC and HCO^+ are fitted with single Gaussians. ASAP estimates the Gaussian parameters and associated uncertainty from the noise in the spectra. Fitting results for a typical PSW spectrum towards G301 are shown in Figure 1. This observation is typical in the sense that it is the closest to the median in $T_{\rm sys}$ (179 K) and elevation (50.37°).

PASA, 30, e038 (2013)
doi:10.1017/pasa.2013.18

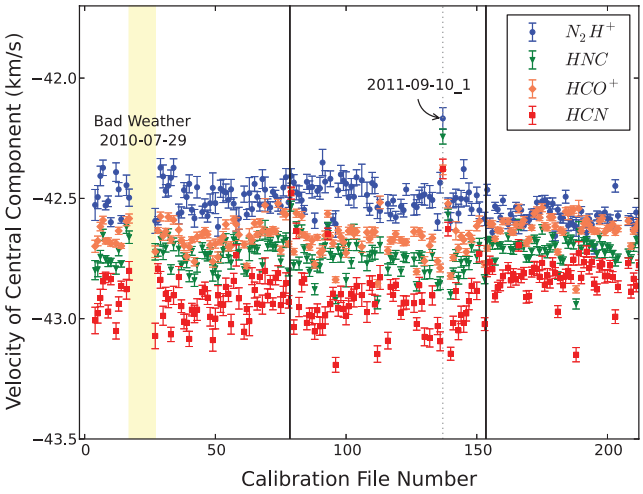

Figure 2. The velocity of the central component for each of the four transitions as a function of sequential file number (effectively time). N_2H^+ is shown as (blue) circles, HNC is shown as (green) triangles, HCO^+ is shows as (orange) diamonds, and HCN is shown as (red) squares. Black vertical lines delimit the breaks between our three observing seasons. Additional features are marked and discussed in the text.

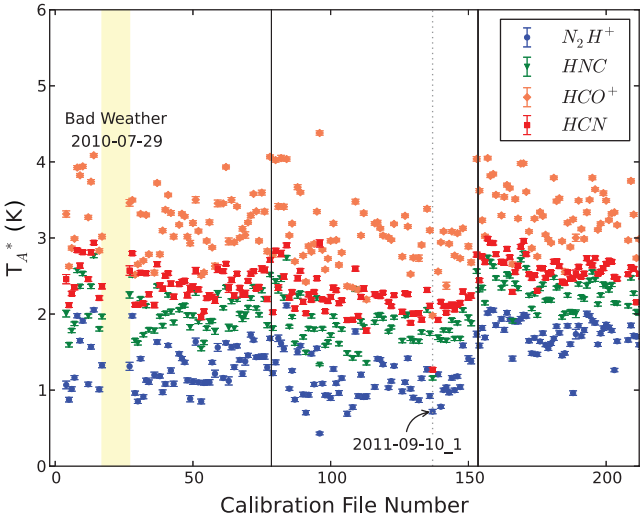

Figure 3. The amplitude of the central component (if there are multiple components) for each of the four main transitions as in Figure 2.

Spectra in the maps were fitted using SPECFIT within CASA,[4] with the same parameters as for the PSW observations. SPECFIT produces output maps of the fit parameters and automatically masks pixels within the map that fail to produce a reliable fit. HNC and HCO^+ are reliably fitted over most of the map, while N_2H^+ and HCN are only reliably fitted over the central portion of the map.

4 DATA DESCRIPTION

4.1 Position-switched data

Tables describing the PSW observations of G301 and our Gaussian fit parameters are given in the Appendix. In the rest of the analysis, we consider only observations for which the fit parameters were well determined according to the following criteria. For a given molecular transition, n, we require that the amplitude a and the fit uncertainties on the amplitude and velocity (σ_{a_n} and σ_{v_n}) obey the following:

$$a_n > 0, \tag{1}$$

$$\sigma_{a_n} < 0.2\,\mathrm{K}, \tag{2}$$

$$\sigma_{v_n} < 0.07\,\mathrm{km\,s^{-1}}. \tag{3}$$

Figures 2 and 3 show the central velocity and the amplitude of the central component for each of the main four transitions. These figures only include days for which the fits to all four transitions met the reasonable fit criteria defined in equations (1)–(3). These plots omit entries where the fit failed, based on criteria for reasonable parameters, but it does not specifically exclude data taken under poor weather conditions (as reported by high $T_{\rm sys}$ values), although the criteria restricting the uncertainty on the fit parameters effectively eliminate data taken at high $T_{\rm sys}$.

Both figures exhibit a significant change near the start of the third season. This is not indicative of true source variability. Rather, during the third observing season, we started observations consistently at a later LST (local sidereal time), so that G301 was at a higher elevation and later time-of-day when it was observed. Variations in gain with elevation are common in radio telescopes and variations in gain as a function of time-of-day are also expected, particularly for a dish which is not temperature controlled (as is the case for the Mopra telescope dish); the gain variation is induced by variations in the thermal lag of structural members of the telescope (Doyle 2009). In general, the dish will tend to lose shape (and therefore efficiency) when the temperature has recently changed rapidly (shortly after dusk and dawn).

As discussed later, at low elevation there is evidence for a systematic offset in the pointing model, and this systematic offset accounts for the change in the behaviour of the velocity in Figure 2. This is a result of strong velocity gradients in our map of G301 which are significantly different for different transitions.

The amplitudes and velocities of different transitions are highly correlated. That is, if the amplitude of HNC is greater than average, the amplitude of N_2H^+ will also be greater than average. We can quantify this with the correlation coefficient between the amplitudes of pairs of transitions. For example, the correlation coefficient between the amplitudes of N_2H^+ and HNC is 0.91, which is typical for the pairwise correlation coefficient of amplitudes in our data. This suggests that systematic trends in the gain of the Mopra telescope rather than purely random effects are producing the amplitude variation.

[4] http://casa.nrao.edu/

We note two other features of these data. First, there is a significant gap between file numbers 17 and 27, which appears marked with a yellow band in Figures 2 and 3. These missing points correspond to a series of observations taken under poor weather conditions on 2010 July 29, with $T_{sys}>$ 500 K. Normally we did not attempt to observe during such bad weather conditions but during this session, near the start of the survey, we continued to attempt to observe G301. Several of these observations resulted in detectable line emission, but the fits are often poorly constrained, and thus do not meet our quality criteria in equations (1)–(3) and are not included.

The second feature of note is the behaviour of points at file number 137, taken on 2011 September 10. These observations are labelled in Figures 2 and 3 and a light grey dotted line is plotted to help guide the eye. This observation was taken during extremely windy conditions (wind speed 35 km h^{-1}) and it is reasonable to think that there were larger than normal pointing error during these observations, resulting in the different velocity and decreased amplitude for the transitions (since the pointed position would be significantly off the peak of emission). This highlights the effect of high winds.

The elevation range of the observations of G301 is strongly bimodal, clustered between 35° and 40° for observations taken at the start of most observing sessions during seasons 1 and 2, and clustered between 55° and 60° for observations taken at the start of observing sessions which started later (including all of season 3). A couple of observations were made at very low elevation (25°–30°) when the shift started earlier than normal, and there are a few observations at intermediate elevations when variations in the schedule, bad weather, or mechanical failure caused us to start observing later. The data are also poorly sampled throughout all times-of-day. Most observing sessions started during the day due to the rise time of the Galactic plane during our observing season. Consequently, there are very few observations of G301 during the night.

There is no systematic trend of peak parameters with T_{sys}. Because G301 was typically observed at higher elevation during the third observing season, the trends seen in Figures 2 and 3 can be partially ascribed to gain variation with elevation. Figure 4 shows the velocity of N_2H^+ and HCN as a function of elevation. These transitions both show a change in velocity with elevation, but in the opposite sense.

It is not possible to disentangle the effects of varying gain as a function of elevation and pointing uncertainty without additional information. Both will tend to decrease the amplitude of the detected emissions, since pointing uncertainty will tend to scatter the observed position away from the brightest point in the source.

4.2 Mapping data

We have three on-the-fly maps of G301. We cross-correlate integrated intensity images of these maps in order to determine their relative positional offsets. We use integrated intensity images of N_2H^+, HNC, HCO^+, and HCN and take the median offsets. The primary purpose of the cross-correlation is to allow us to optimally co-add the maps and produce a map with higher signal to noise for comparing with the PSW data. If the maps were simply co-added based on the positions recorded by the telescope, any errors in pointing would produce a smeared beam in the resultant map.

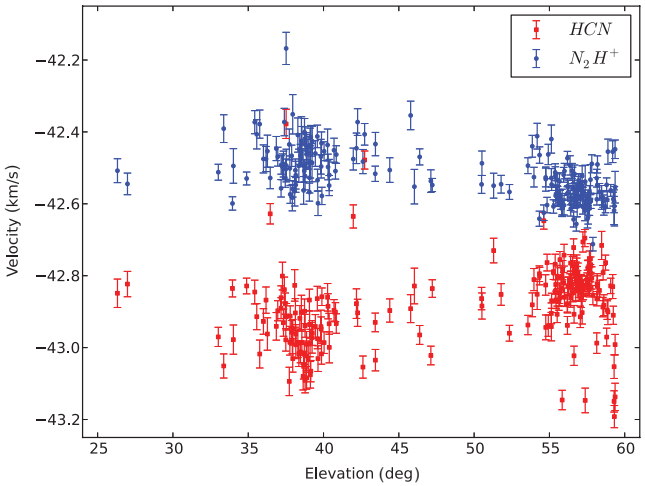

Figure 4. The velocity of the central component for N_2H^+ ([blue] circles) and HCN ([red] squares) as a function of elevation. Significant trends are seen in both N_2H^+ and HCN.

We shift the maps to align with the map taken on 2012 June 29. This map was taken at higher elevation, and thus we assume it will have the lowest absolute pointing uncertainty; we do not have an absolute position reference, but we do not need one for this analysis. Cross-correlation finds the following positional offsets: relative to the 2012 June 29 map, the 2011 May 6 map needs to be shifted by −2.7 arcsec in Galactic longitude and +2.25 arcsec in Galactic latitude; the 2011 August 22 map needs to be shifted by +1.8 arcsec in Galactic longitude and −3.6 arcsec in Galactic latitude.

5 ANALYSIS

Our analysis consists of two distinct steps. First, we use the velocities of the PSW observations to find the most likely location of each observation within our map of G301. This allows us to estimate the pointing reliability of our PSW observations. Second, for each PSW observation, we examine the difference between the observed amplitudes of the transitions and the amplitudes of the transitions at the most likely locations in the map to model. We use the variation in this difference to model and remove the dominant sources of systematic gain variation and to estimate the residual absolute flux uncertainty.

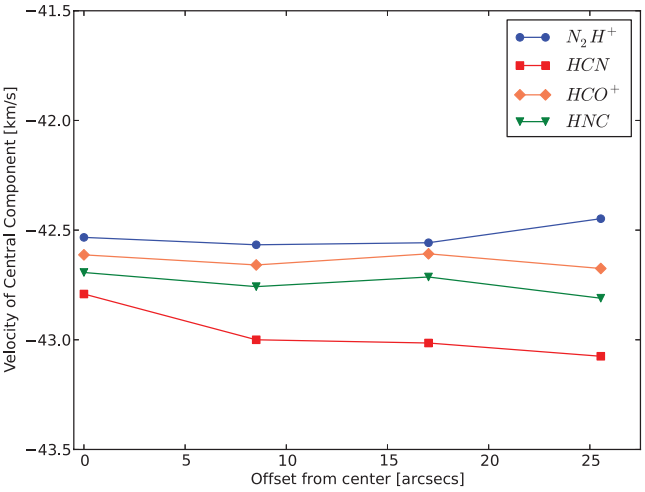

Figure 5. The velocity of the central component for the four transitions along the direction shown in Figure 6, showing opposite gradients in N_2H^+ and HCN and relatively smaller changes in HNC and HCN.

5.1 Most likely location

We use the velocities of the four transitions in the PSW observations to find the most likely location of the observation within our co-added map of G301. That is, we use the velocities in isolation to estimate the pointing reliability. This is valid because systematic gain variations and absolute flux uncertainty will affect only the amplitude of the transitions, and not their velocity. In theory, intrinsic time variability of the source could cause changes in the velocity as well. In addition, errors in the reduction pipeline to derive velocity could contain a dependence on elevation; we examined the possibility that our reduction was incorrectly accounting for Earth's rotation speed (the magnitude of this correction is elevation dependent) but found that this reduction was being performed correctly. Ultimately, the velocity offsets observed in Figure 4 can be well understood by systematic pointing errors, and so we adopt this model as the simplest explanation.

Qualitatively, there is a velocity gradient as one moves to larger Galactic latitudes and smaller Galactic longitudes away from the main clump. Figure 5 shows this gradient along the vector shown in Figure 6. This velocity gradient is large and in opposite directions for N_2H^+ and HCN, and relatively small for HNC and HCO^+. Therefore, an offset in our actual observed position between the points taken at low versus high elevation would produce the behaviour seen in Figure 2.

To find the most likely location within the map of each PSW observation, we seek the location within the map, which minimises the velocity offset of all four transitions simultaneously, subject to a reasonable pointing model. Specifically for our pointing model, we assume that the average position of PSW observations coincides with the nominal targeted position. Furthermore, we assume that the pointing error is independent of angle (ϕ) and therefore that the radial (ρ) distribution of PSW observations can be described by the Rayleigh distribution with a scale factor λ so that

$$P(\rho) = \frac{\rho}{\lambda^2} e^{-\rho^2/2\lambda}. \quad (4)$$

The Rayleigh distribution describes the magnitude of a vector in two dimensions and is the two-dimensional equivalent of the Maxwell–Boltzmann distribution in three dimensions.

Our Bayesian problem is therefore

$$P(\rho, \phi|\text{data}) \propto P(\text{data}|\rho, \phi) \times P(\rho, \phi), \quad (5)$$

for each of i data points. We assume that ϕ is uniformly distributed on the full range $[0, 2\pi]$ and that $P(\rho)$ is given by equation (4) with $\lambda = 10$ arcsec. This prior on ρ comes from the 2013 May 15 version of the Mopra Quick Reference Handbook[5] that estimates the global pointing model as having an 8.3 arcsec rms error in elevation and a 13.0 arcsec rms error in azimuth from an analysis of historical absolute pointing offsets. Ignoring this asymmetry for now, this corresponds to a λ of 10.9 arcsec, which we round to 10 arcsec. Given ϕ and ρ, we assume that our data errors are Gaussian and well represented by the measurement error and thus

$$P(\text{data}|\rho, \phi) \propto \sum_n \left(\frac{v_{m,n}(\rho, \phi) - v_{p,n}}{\sqrt{\sigma_{p,n}^2 + \sigma_{m,n}^2}} \right)^2, \quad (6)$$

for each (n) of the four transitions (N_2H^+, HNC, HCO^+, HCN), v_m refers to the velocity observed in a map pixel (x, y) at some distance ρ and angle ϕ from the peak of the map, v_p refers to the velocity obtained from the PSW observation, and σ_p and σ_m refer to the formal fit uncertainty on the velocity of the PSW observation and the velocity at a given map pixel, respectively.

We calculate equation (6) for each point in our maps of G301 and assign each PSW observation a most likely position based on the map pixel that maximises this probability. We do this both for the original maps and for interpolated maps, where we interpolate down by a factor of four in both x and y. We find that using the interpolated map allows us to well reproduce the observed PSW velocities.

The most likely location of each PSW observation is shown in Figure 6 on each of the four main transitions. Some jitter is added to each point in this display in order to better visualise the density of points. These results show that the PSW observations taken at high elevation ($z > 45°$) align quite well with the centre of this map (effectively taken at high elevation, since maps were shifted to align with the map taken on 2012 June 29 at elevation 58°–60°), but that some of the points at lower elevation show a systematic offset towards larger Galactic latitude and longitude. The best-fit location for a small number of points is significantly farther from

[5] http://www.narrabri.atnf.csiro.au/mopra/Mopra_QRH.pdf

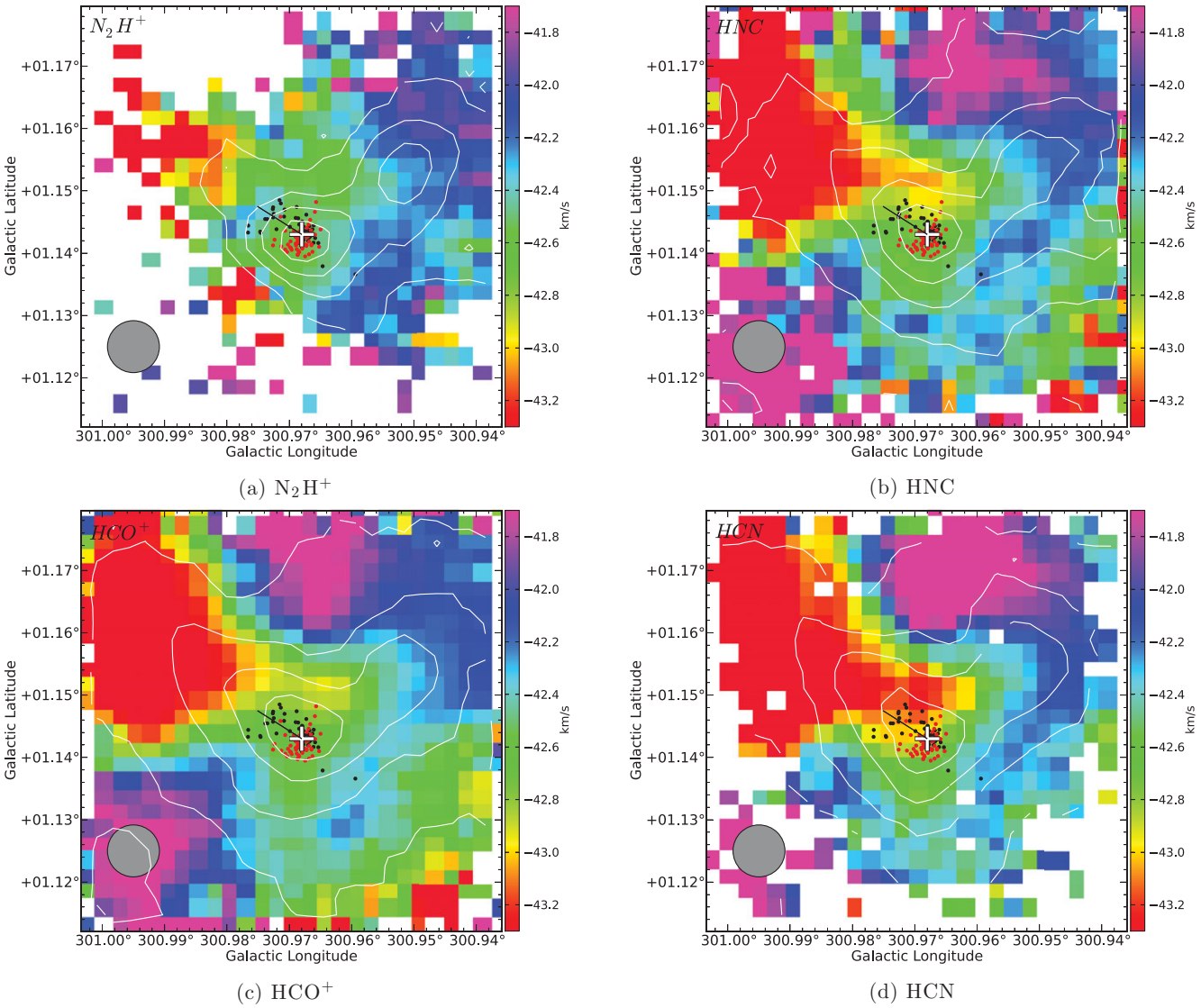

(a) N_2H^+ (b) HNC

(c) HCO^+ (d) HCN

Figure 6. The most likely positions of all PSW observations on a map of G301, derived by matching the velocities of all four main transitions simultaneously. In each panel, the colour scale shows the velocity of the central component of the transition, and the contours show the amplitude of the central component of that transition (with contours at 20%, 40%, 60%, and 80% of the maximum value). The black and red points show the most likely position of each observation, red for observations taken above 45° of elevation and black for observations below that. A small amount of random jitter is added to each point to improve the display. The white cross shows the nominal position for the PSW observations. The beam of the Mopra telescope at 90 GHz is shown in grey. The black line shows the vector displayed in Figure 5.

the centre of the map. These points correspond to PSW observations with significantly discrepant velocities; the PSW observation on 2011 September 10 highlighted in Figure 2 is one of these points.

5.2 Systematic amplitude variation

With these most likely locations determined, we proceed to consider the systematic amplitude variations seen in the PSW observations of G301. We assume that G301 has no significant intrinsic time variability and that all variation is due to gain variations. We expect that the Mopra telescope will experience some gain variation as a function of elevation, and also that the Mopra telescope may display some gain variation due to the fact that the dish is not kept at a constant temperature. This latter problem is exacerbated by the fact that observations were taken at different times during the day as well as over the course of many months during one observing season. The Mopra telescope could therefore be changing shape as the Sun warms the dish each day and as the ambient temperature changes during the season. One source of systematic variation can be discounted; no pointing model changes or receiver re-calibrations were performed during these three observing seasons.

We perform this analysis in two parts. First, we examine the data to find the dominant systematic variations. The goal

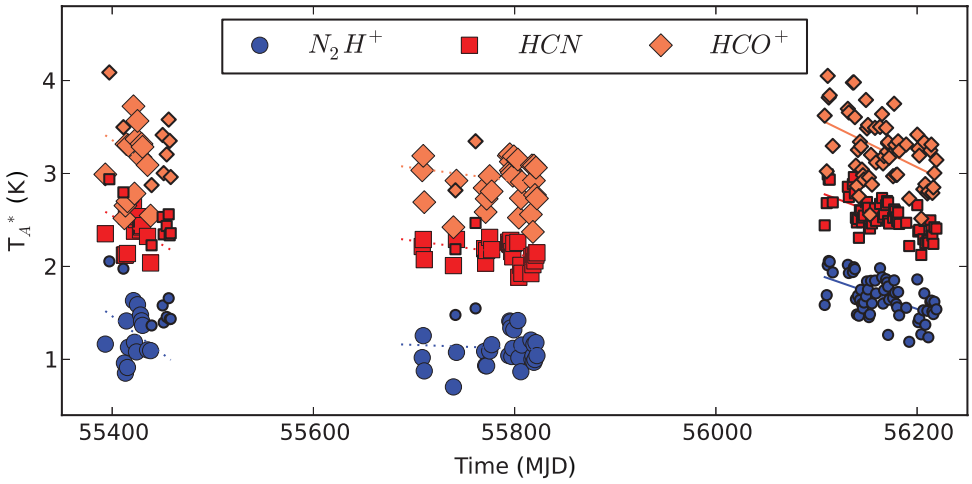

Figure 7. The flux for three of our four main transitions (HNC omitted for clarity) for PSW observations where $T_{\rm sys} < 180$ K. The time range is displayed as the modified Julian date (MJD) and covers from 2010 July to 2012 October. Points are coded by colour and shape based on the transition observed, and are sized based on whether the observation was conducted at high elevation ($z > 45^\circ$; small points) or low elevation ($z < 45^\circ$; larger points). Lines show linear fits to the trend within each year. Large mean amplitude variations between observing seasons are apparent, as well as trends within each observing season.

is not to fully explain the absolute flux variation, but to identify the major systematic variations and quantify the remaining absolute flux uncertainty. Based on this examination, we construct a hierarchical Bayesian model which allows us to coherently account for multiple sources of uncertainty and gain variations at the same time.

5.2.1 Examination of amplitude variation

In order to simplify our search for the dominant systematic variations, we examine only the subset of our data taken during good observing conditions ($T_{\rm sys} < 180$ K) and for which the best-fit position determined above is within 21 arcsec of the centre of the map (which corresponds to where the amplitude of the transition is affected by less than 10% due to pointing error). These data are shown in Figure 7.

There are significant variations within each observing season as well as significant jumps between observing seasons. Within each observing season, we fit a line to the amplitude of the molecular transition versus time. The amplitude decreases during the first and second seasons, but not with a high degree of statistical significance (1–2σ). In contrast, the decline is highly significant (6σ) during the third season. All transitions show similar slopes. The fits for the first and second observing seasons are fitted only to the points taken at low elevation, so as to avoid any variation produced by gain–elevation effects. The magnitude of the jump in amplitude from the second to the third seasons is large (0.5 K), but the data taken during the third observing season were all taken at high elevation, in contrast to the previous two seasons.

One explanation for these trends is that the gain of the Mopra telescope at 90 GHz decreases during the course of an observing season. During the first observing season, this trend is partly obscured by the fact that later in the season we began observing sessions later, and thus observed G301 at higher elevation. A dependence of the gain on elevation is physically well motivated and explains the rise at the end of the first observing season and the relatively higher transition amplitudes observed during the third season.

The third observing season contains particularly robust evidence for a decrease in transition amplitude from the start to the end of the observing season. Figure 8 shows some possible explanatory variables, including elevation, temperature, and time-of-day (calculated as the number of hours since sunrise). This figure shows the difference between the PSW amplitude and the amplitude of the map at the most likely location versus the time (in seconds) since May 1. We choose May 1 as our reference time for a season so that all three observing seasons can be put on the same time axis when examining seasonal trends. This difference is offset from zero and linearly decreasing with time; error bars on the amplitude are smaller than the plot symbols. Linear fits to these relations show no significant structure in the residuals. This trend is not due to changes in elevation; our observing session start times were at roughly constant local sidereal time, so that G301 was at a similar elevation throughout the observing season. There is a negative correlation with ambient temperature ($\rho = -0.41$) and a positive correlation with the time-of-day ($\rho = 0.52$); the correlation is stronger with time-of-day. From this, we conclude that the dominant variations in the telescope gain can be modelled as due to elevation and time-of-day (as a proxy for thermal deformation).

One complication of using time-of-day to explain the observed decrease during an observing season is that the real physical explanation of the decreased gain is likely deformation of the telescope due to differential thermal lag between components. This deformation will typically be most

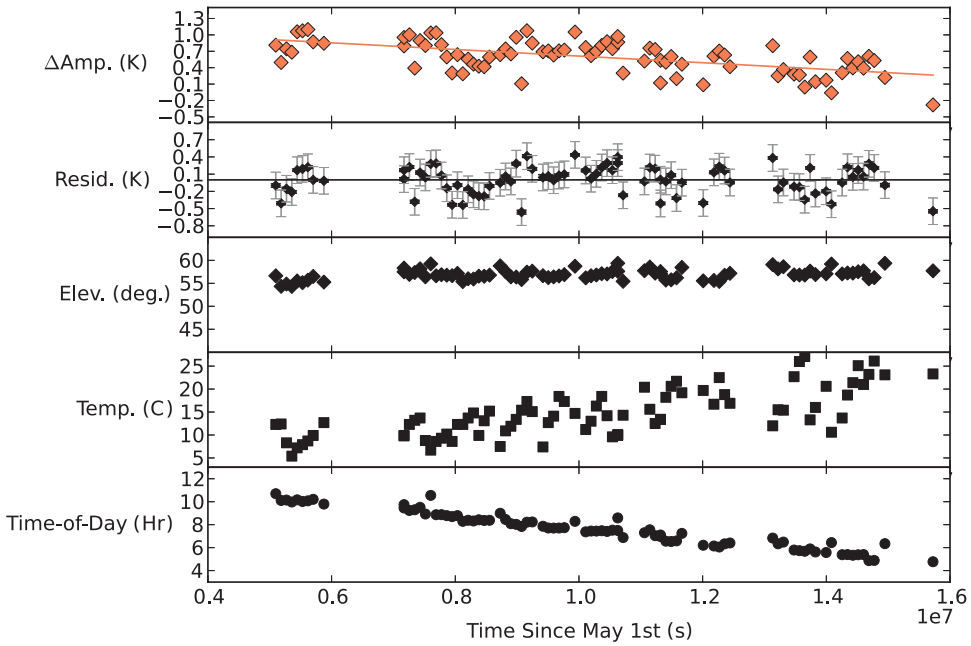

Figure 8. A closer examination of the time variability of the HCO^+ transition amplitude during the third observing season. Top row: the difference between the amplitude of a molecular transition in a PSW spectrum and the amplitude of that transition most likely location within the reference map. Second row: residuals of the above linear fit; grey error bars show the inferred absolute flux uncertainty. Third row: elevation is roughly constant. (Fourth and fifth rows: there is a trend with ambient temperature and with the time-of-day; the correlation is better with time-of-day.

significant shortly after dusk and dawn, when the temperature is typically changing most quickly. We examined the ambient (air) temperature at the Mopra telescope site in the hours preceding each PSW observation, but were unable to find a variable based on fitting these temperature profiles that produced a good correlation with the amplitude trend seen in Figure 8. One possible reason for this is that the temperature of the dish (which is not measured directly) is strongly influenced by illumination by the Sun, and time-of-day is the best proxy available for this effect.

The third observing season data shown in Figure 8 do not include any points taken more than 12 h after sunrise (after the trimming of low-quality data described in Section 4.1); the handful of points taken during the night are from the other two observing seasons. We thus do not have adequate coverage during the night to model this relationship, and therefore we exclude these points and focus on those taken less than 12 h after dawn, where our data provide good coverage.

5.2.2 Model

For any given transition, we assume that the measured amplitude for any PSW observation, a_p is generated as

$$a_p = \tilde{a}_m \times \eta(t) \times \zeta(z) + \epsilon_p + \epsilon_f, \tag{7}$$

where $\tilde{a}_m$ is the true amplitude of the transition at the position where the telescope was pointed within the map (as determined from minimising equation (6)), $\eta(t)$ is the gain factor as a function of time-of-day (t), $\zeta(z)$ is the gain factor as a function of elevation (z), ε_f is the remaining absolute flux uncertainty, and ε_p is the measurement error for the amplitude of an individual PSW observation. We assume that $\varepsilon_f \sim N(0, {\sigma^2}_f)$ and that $\varepsilon_p \sim N(0, {\sigma^2}_p)$, where σ_p is our estimate of the uncertainty on a_p and σ_f characterises the absolute flux uncertainty.

We further assume that both gain factors are linear functions of their dependent variables and normalised such that they are equal to unity at the elevation and time-of-day of our reference map (t_0, z_0) so that

$$\eta_n(t) = 1 + \beta_n \times (t_p - t_0), \tag{8}$$

and

$$\zeta_n(z) = 1 + \delta_n \times (z_p - z_0), \tag{9}$$

where t_p and z_p are the time-of-day and elevation of each PSW observation. The elevation and time-of-day are the same for each of the n species, but the model allows for different gain factors for each of our four main transitions, hence the subscripts on β_n and δ_n.

In the case of elevation, gain–elevation effects are often represented by a more complex function, since efficiency normally peaks around $z = 45°$–$60°$, and drops at higher and lower elevation. However, the data are strongly clustered in two narrow elevation ranges, so a higher-order function cannot reliably be fit. This fit should be used cautiously, and certainly not extrapolated to elevations outside of the measurements (i.e. $z > 60°$ or $z < 30°$). Likewise, the data

only cover between 3 and 12 h after sunrise; over this period of time, the gain of the Mopra telescope appears to respond roughly linearly, but this fit should not be extrapolated outside of this time range.

Unfortunately, we do not have $\tilde{a}_m$, only an estimate, a_m, from a noisy map:

$$\tilde{a}_m = a_m + \epsilon_m, \tag{10}$$

where $\varepsilon_m \sim N(0, {\sigma^2}_m)$; therefore, we have the following generative model for each PSW observation, a_p:

$$a_p = [a_m + \epsilon_m] \times \eta(t) \times \zeta(z) + \epsilon_p + \epsilon_f. \tag{11}$$

We use the map of G301 taken on 2011 August 22 as our reference map, as it was taken at values of t_0 and z_0 near the median of our PSW observations. Specifically, $t_0 = 5.5$ h and $z_0 = 44°$. Recall that we used the combined map to find the most likely location of each observation based on matching velocities. Those positions (appropriately shifted) are used to look up the amplitudes in this single map of G301, which has a well-defined t and z associated with it (which the combined map does not).

We now compute inferences on our parameters of interest, β_n, δ_n, and σ_f, which represent the gain corrections for elevation and time-of-day and the absolute flux uncertainty. We assume uniform priors for β_n, δ_n, and σ_f. We use PYMC[6] to compute the posterior probability distribution for each of these parameters, using adaptive Metropolis–Hastings sampling (Haario, Saksman, & Tamminen 1998). The traces converge well, and the posterior probability distributions are symmetric and single valued, allowing us to specify the results simply as approximate Gaussians.

6 RESULTS

6.1 Pointing uncertainty

The best estimate of the pointing precision comes from matching the velocities derived from the spectra of the PSW observations against the velocities across the map. This gives a median position of l, b = (300.9678°, 1.1440°) and a radial scatter of 9.8 arcsec at $z < 45°$ and a median position of l, b = (300.9678°, 1.1421°) with a radial scatter of 4.3 arcsec at $z > 45°$. The Galactic positions given above are not absolute, but are relative to the map of G301 taken on 2012 June 9 at z = 59°. This corresponds to an offset of 6.8 arcsec in Galactic latitude between the median positions at the two elevation ranges, and suggests that there could be a systematic bias in the pointing of the Mopra telescope at different elevations. These results are modestly dependent on our choice of prior on ρ in equation (4). In particular, decreasing λ to less than 5 arcsec removes the offset between observations at low and high elevation as all best-fit locations are now forced to be quite close to the nominal pointing centre. Increasing λ to 20 arcsec has a small effect on our estimate of the pointing precision, increasing our estimate of the pointing uncertainty by 2 arcsec.

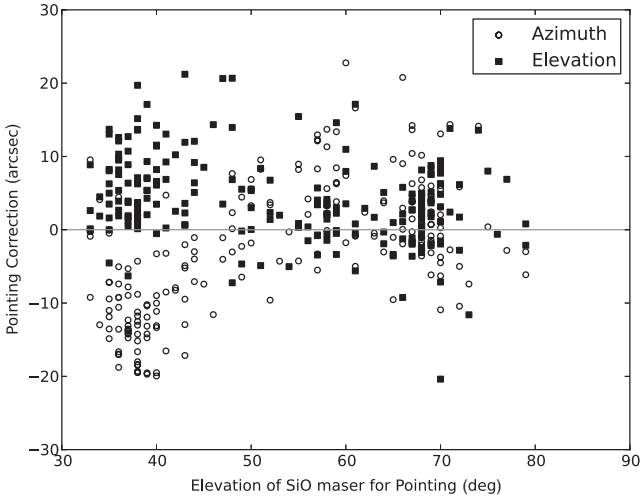

Figure 9. Pointing corrections derived from observing an SiO maser immediately after observing G301. Corrections in both azimuth and elevation are significant below an elevation of 45°and small above this elevation.

The estimate for pointing uncertainty is therefore not fully encapsulated in a single number. At low elevation ($z < 45°$), we infer a random scatter of 10 arcsec, but with a systematic offset of about 7 arcsec. At high elevation ($z > 45°$) the Mopra telescope is relatively more precise, with a pointing uncertainty of 6 arcsec. For the full set of points (at all elevations), the radial scatter in inferred positions is 8 arcsec.

An additional check on these pointing results is made by considering the corrections to the pointing model required after a PSW observation of G301. As mentioned in Section 2.1, we performed a pointing correction on an SiO maser immediately after a PSW observation of G301. The estimate of our pointing uncertainty derived in this fashion broadly agrees with our results from matching velocities. Figure 9 shows the corrections as a function of elevation of the SiO maser (all observations were in a fairly narrow range of azimuth). At low elevation ($z < 45°$), there is a systematic correction of 6 arcsec in elevation and −11 arcsec in azimuth. The standard deviation of these corrections is 6 arcsec in elevation and 5 arcsec in azimuth. At higher elevation ($z > 45°$), the average correction is small (2 arcsec in elevation and azimuth) and the standard deviation of these corrections is 7 arcsec in elevation and 6 arcsec in azimuth. The systematic pointing offsets at low elevation deduced from matching velocities correspond to offsets of 5 arcsec in elevation and −8 arcsec in azimuth (at the position of G301 and at the typical local sidereal time of G301 PSW observations), so this offset is in excellent agreement. The standard deviations of these corrections (expressed as radial corrections) are 8.2 and 8.8 arcsec for the two elevation ranges respectively. This is also in excellent agreement with our inferred overall pointing error of

[6] http://pymc-devs.github.io/pymc/

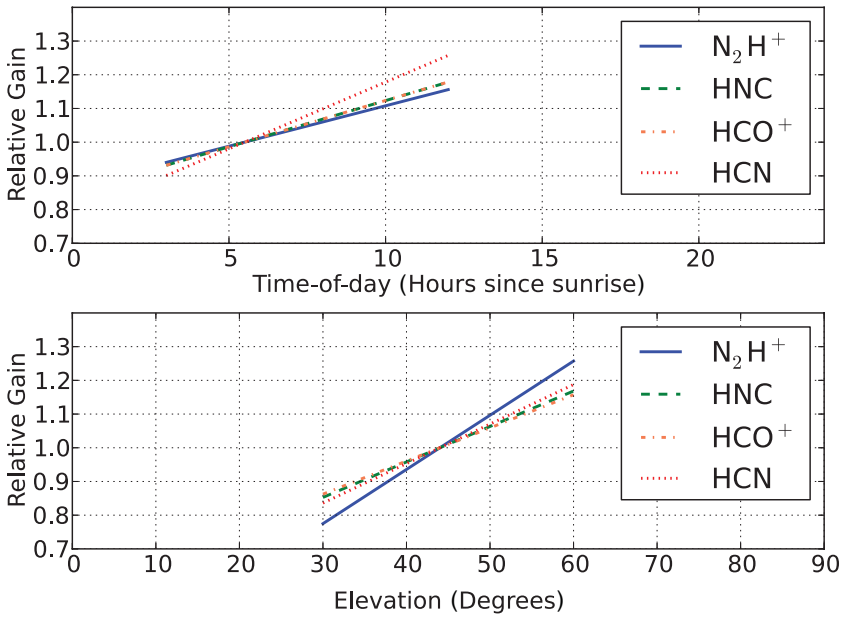

Figure 10. Gain of the Mopra telescope at 90 GHz (normalised to unity at $t_0 = 5.5$ h and $z_0 = 44°$) as a function of time-of-day (top) and elevation (bottom) for the four main transitions in this study (N_2H^+, HNC, HCO^+, and HCN). Relations are shown only for the ranges of parameters where they are calibrated by our observations of G301, and may deviate significantly from these linear fits outside of these ranges.

Table 3. Gain curves.

Line	$\sigma^a{}_i$ (K)	β (h^{-1})	δ (deg^{-1})	$\sigma^b{}_f$ (K)
N_2H^+	0.38(2)	0.024(9)	0.016(2)	0.26(2)
HNC	0.34(1)	0.028(6)	0.010(1)	0.24(1)
HCO^+	0.43(2)	0.028(6)	0.010(1)	0.36(2)
HCN	0.29(2)	0.040(7)	0.012(2)	0.28(2)

[a] Absolute flux uncertainty before accounting for systematic gain variations.
[b] Absolute flux uncertainty after accounting for systematic gain variations.

9 arcsec. This analysis confirms our belief that the pointing is more accurate at high elevation.

Our estimate for the pointing uncertainty of the main MALT90 maps is 8 arcsec, comparable to the value of 10 arcsec often quoted for the Mopra telescope (e.g. Foster et al. 2011; Jones et al. 2012). Since the pointing model seems to also be more accurate at high elevation, then it could be the case that MALT90 survey maps taken at high elevation have a pointing uncertainty of only about 6 arcsec.

6.2 Gain factors

Table 3 lists our inferred parameters and 1σ uncertainties from our modelling of two factors influencing the gain of the Mopra telescope at 90 GHz, $\eta(t)$ where t is the time-of-day (number of hours since sunrise) and $\zeta(z)$, where z is the elevation in degrees. These relations are described in equations (8) and (9). Both these gain relations are normalised to be one at the time-of-day and elevation of our reference map ($t_0 = 5.5$ h and $z_0 = 44°$), and describe how the gain of the Mopra telescope changes in our PSW observations taken at different times-of-day and elevations. Figure 10 visualises these relations over the ranges where the explanatory variables (elevation and time-of-day) are well sampled in our observations of G301.

All the gain versus elevation relations (δ in Table 3) are consistent with each other at the 3σ level. Taking N_2H^+ as an example, the relation implies that at 30° of elevation, the observed flux would be only 78% of the baseline flux observed at 44°, while the flux would be 126% of the baseline at 60°. The relation is not calibrated outside of this elevation range, and should not be used at lower or higher elevations. In particular, we expect that the gain might peak around 60° of elevation (based on other telescopes) and thus extrapolating this linear relation to higher elevations would produce dramatically incorrect answers.

The gain variation with time-of-day relations is also (2σ) consistent with each other. For N_2H^+, the slope of this gain relation is less than 3σ different from zero, but the slope is more than 4σ significant for all the other transitions. The effect is strongest in HCN. This is somewhat counterintuitive in our picture, where temperature deformation of the dish changes the efficiency of the telescope. In particular, since HCN is at the lowest frequency of our transitions, it would generally be the least sensitive to gain variation due to deformation of the dish (although the frequency difference is not large). Nonetheless, the relatively large uncertainties on

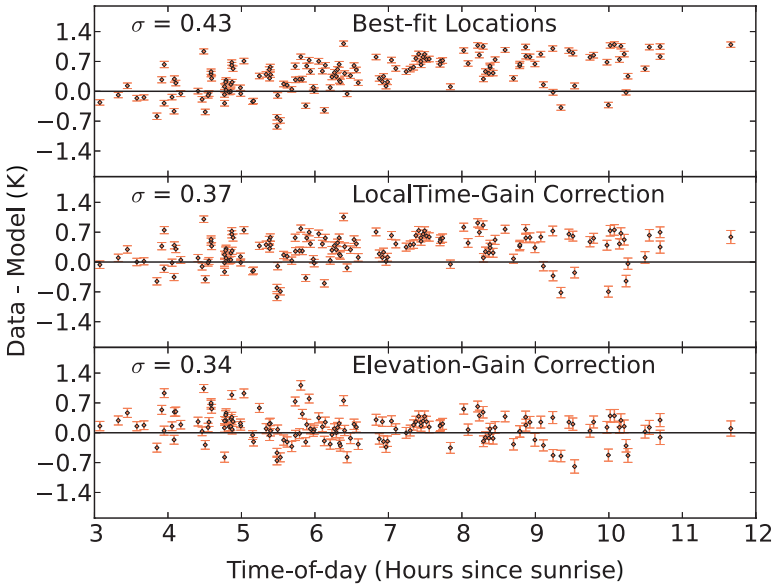

Figure 11. Residuals of our model explaining the amplitudes of PSW observations of HCO^+ after including various refinements. Top row: the amplitude difference from the most likely location in the map. Middle row: residuals after including the gain variation with time-of-day. Bottom row: residuals after also including the gain variation with elevation.

these relations mean that the four relations are all consistent with each other. Relative to a baseline observation taken at 5.5 h past sunrise, the model implies that for HCO^+one would observe a flux of 118% of the baseline flux at 12 h past sunrise and a flux of 93% of the baseline flux at 3 h past sunrise. This relation is not calibrated outside of this range.

After accounting for these first-order effects, there is still more variation in the PSW observation amplitudes than can be accounted for by noise in the spectrum and its resultant uncertainty on the fitted amplitudes. Our model captures this number as an additive Gaussian noise term characterised by σ_f in Table 3, although this could also be modelled as a (multiplicative) variation in gain. The absolute magnitude of this variation is 0.24 ± 0.1 K for HNC and 0.26–0.36 ± 0.2 K for N_2H^+, HCN, and HCO^+. Using typical transition amplitudes of $N_2H^+ = 1.5$ K, HNC = 2 K, $HCO^+ = 3.5$ K, and HCN= 2.5 K, these variations can be expressed as percentage variations of 17%, 12%, 10%, and 11%, respectively. This roughly follows our expectation that the absolute flux uncertainty would be a function of frequency, and be worst at high frequencies (i.e. the flux accuracy for N_2H^+at 93 GHz is worse than the other transitions between 88 and 91 GHz).

By contrast, the following numbers describe the standard deviation of the PSW observation amplitudes without accounting for these first-order effects (σ_i in Table 3). For N_2H^+, $\sigma_i = 0.38$ K, for HNC, $\sigma_i = 0.34$ K, for HCO^+, $\sigma_i = 0.43$ K, and for HCN, $\sigma_i = 0.29$ K. As percentage variations, these are roughly 25%, 17%, 12%, and 12%, respectively. Correcting for the first-order changes in the Mopra telescope's gain at 90 GHz therefore produces a modest, but significant, improvement in the absolute flux calibration of the data.

These flux uncertainties are much larger than the fitting uncertainty for our amplitudes in our PSW data (typical $\sigma_a =$ 0.03–0.05 K) and in our maps ($\sigma \sim$ 0.05–0.08 K for a typical MALT90 map). This uncertainty sets a limit on the precision of our transition parameter determinations using the MALT90 data. We expect that the absolute flux uncertainty is a slowly varying function of time. Therefore, within a map, one does not have to take into account this absolute flux uncertainty when measuring relative quantities, such as the 50% contour of emission in a given molecular transition within a source. In addition, because of the strong correlation among molecular transition amplitudes, we expect that this residual flux uncertainty is frequency independent (at least in sign, if not exactly in amplitude) and thus the fact that MALT90 maps of different species are made concurrently should remove most of this absolute flux uncertainty when looking at, for instance, molecular transition ratios from one source to another.

Our model is shown in Figure 11, which displays the molecular transition amplitudes from the PSW data minus the model amplitudes after including a series of refinements, which include (1) taking the molecular transition amplitude from the most likely location in the reference map, (2) including gain variation with time-of-day, and (3) including gain variation with elevation. This plot shows all three seasons of HCO^+ together, and the error bars include the uncertainty from our model parameters. The unweighted standard deviation of these points decreases with each refinement to the model.

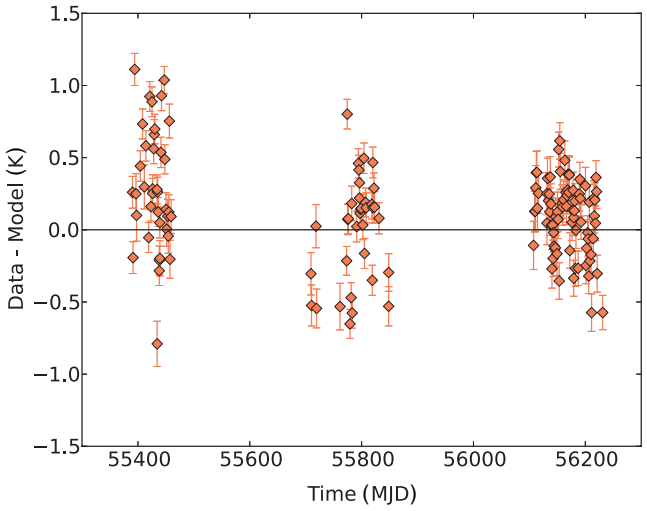

Figure 12. Residuals of our model explaining the amplitudes of PSW observations of HCO^+ versus time expressed as MJD. This residual is equivalent to the bottom panel of Figure 11. Any intrinsic source variability is less than the magnitude of our systematic corrections.

6.3 Intrinsic source variability

Figure 12 shows that there is still some residual variation between seasons, although it has been much reduced (cf. Figure 7). These variations would be statistically significant if not for the systematic nature of our gain corrections (Section 6.2). That is, comparing the mean and standard error on the mean for the second observing season (-0.16 ± 0.02 K) and the third observing season (0.04 ± 0.01 K) appears to show a statistically significant difference. However, since most of the third observing season spectra were taken at high elevation (55°–60°) while most of the second observing season points were taken at low elevation (35°–45°), the systematic correction for the elevation–gain relation is roughly 0.5 K, far larger than the residual difference.

This variation could still hint at intrinsic source variability, but it could also be simply another instrumental systematic not fully modelled in this work. The underlying physical explanation for this variability could be systematically different in different observing seasons, and therefore intrinsic source variability at this level (0.3 K or 10%) cannot confidently be measured. The data would be sensitive to much larger intrinsic source variability, such as the 40% (continuum) flux variation seen in a UC H II region by e.g. Franco-Hernández & Rodríguez (2004). If G301 exhibited a similar flux variability in line emission, this would produce roughly a 1.4-K change in the brightness of the HCO^+ transition, a variation to which the data would be sensitive. Continued monitoring of this source will help us to constrain the magnitude of any intrinsic source variability.

7 CONCLUSIONS

We have presented the MALT90 data for this survey's characterisation source, G301, a well-studied UC H II region. Repeated PSW observations of this source (at the start of each observing session over three seasons of the survey), in combination with a high-quality map of this source, allow us to characterise the system performance of the Mopra telescope at 90 GHz, and thus several parameters describing the repeatability of measurements and the pointing reliability of the MALT90 survey.

We see strong systematic time variability in the amplitudes of transitions in our single-point observations of G301, but we do not believe that this is due to intrinsic source variability. Instead, the long-term amplitude trends can be explained by a model in which the Mopra telescope at 90 GHz has two significant gain variations, one as a function of time-of-day (probably related to temperature fluctuations), and one as a function of elevation. To first order, the variation within an observing season is due to changes in the time-of-day as our observing session starts when the Galactic plane rises. The variation between the first two seasons and the third season is due to elevation (since the third observing season started at later local sidereal time).

Our main results characterising the survey are as follows:

- We estimate our pointing uncertainty to be 8 arcsec. This number includes a systematic offset between observations taken at different elevations, with observations at low elevation likely to be mis-pointed. The pointing uncertainty is only 6 arcsec for sources observed above 45° of elevation (the majority of MALT90 sources).
- We quantify the gain–elevation relation for the Mopra telescope at 90 GHz (Table 3 and Figure 10). The strong clustering of our observations in two small elevation ranges (around 35°–40° and around 55°–60°) prohibits us from fitting anything of higher order than a linear relationship and limits the range over which such a correction can be applied.
- We infer that the Mopra telescope at 90 GHz experiences gain variation as a function of time-of-day. In particular, efficiency increases linearly during the day from 3 to 12 h after sunrise. This variation is not characterised outside of this time period. The gain relations are consistent for the four different transitions used in this analysis.
- After removing these two sources of gain variation, there is a remaining absolute flux uncertainty of 0.24–0.36 K or 10%–17% depending on the transition in question. Without this correction, the absolute flux uncertainty is 0.29–0.43 K or 12%–25%. This systematic uncertainty dominates over the noise inferred from examining signal-free sections of the spectra. For certain applications, this sets the uncertainty of MALT90 molecular transition amplitudes, although for others (i.e. line ratios) the strong correlations among transition amplitudes and the fact that all the molecular transitions are observed simultaneously minimising this source of uncertainty.

We do not use our estimates of these systematic gain variations to correct the fluxes in the MALT90 survey. The primary reason is that our observations of G301 do not adequately span the elevation and time-of-day ranges present in our full dataset; a correction of the full set of survey maps would therefore involve significant extrapolation. In particular, our observations of G301 only well sample two small ranges in elevation (35°–40°and 55°–60°) and only well sample the range from a few hours after sunrise to just after sunset.

A second reason is that not all MALT90 maps can be characterised by a single elevation or time-of-day. Although most sources were observed during a contiguous block of time (that is, the map scanning in Galactic latitude immediately followed the map scanning in Galactic longitude), for some sources we observed the two different scan maps at discontiguous times for a variety of reasons. The most common cause was only finishing a scan map in one direction for the last source of a given observing session. Under the normal data reduction pipeline, maps are combined with $T_{\rm sys}$ weighting; to apply the elevation and time-of-day corrections presented here would require an additional weighting factor before co-addition. For both these reasons, we present the MALT90 data without these corrections applied. Nevertheless, these corrections are important to understand for reliable analysis and interpretation of MALT90 data and we encourage their use where appropriate.

The characterisation of telescope parameters such as the pointing uncertainty, absolute flux calibration, and gain-variation relations will be useful for other users of the Mopra telescope at 90 GHz, since MALT90 observes in a fairly standard fashion. We will continue to monitor G301 as part of the MALT90 survey, including observations at a broad range of elevations and times-of-day, and present updated values for these parameters with the final data release paper. In addition, increased observations will hopefully allow us to break the degeneracies among observing season, elevation, and time-of-day and thus place strong upper limits on any intrinsic variability of molecular transitions in UC H II regions such as G301.

ACKNOWLEDGEMENTS

We thank the referee, Michael Burton, for useful suggestions which improved the paper. The Mopra telescope is part of the Australia Telescope National Facility and is funded by the Commonwealth of Australia for operation as a National Facility managed by CSIRO. The University of New South Wales Mopra Spectrometer Digital Filter Bank used for the observations with the Mopra telescope was provided with support from the Australian Research Council, together with the University of New South Wales, University of Sydney, Monash University, and the CSIRO. The authors also thank the staff of the Paul Wild Observatory for their assistance during these observations. The MALT90 project team gratefully acknowledges the use of dense clump positions supplied by ATLASGAL. ATLASGAL is a collaboration between the Max Planck Gesellschaft (MPG: Max Planck Institute for Radioastronomy, Bonn, and the Max Planck Institute for Astronomy, Heidelberg), the European Southern Observatory (ESO), and the University of Chile. J.M.J gratefully acknowledges funding support from NSF grant AST-1211844.

REFERENCES

Caswell, J. L. 1997, MNRAS, 289, 203
Caswell, J. L. 2003, MNRAS, 341, 551
Caswell, J. L., Kramer, B. H., & Reynolds, J. E. 2009, MNRAS, 398, 528
Chapman, J. F., Millar, T. J., Wardle, M., Burton, M. G., & Walsh, A. J. 2009, MNRAS, 394, 221
Chin, Y.-N., Henkel, C., Whiteoak, J. B., Langer, N., & Churchwell, E. B. 1996, A&A, 305, 960
Churchwell, E. 1999, in NATO ASIC Proc. 540: The Origin of Stars and Planetary Systems, ed. C. J. Lada & N. D. Kylafis (Kluwer: Academic Publishers), 515
Contreras, Y., et al. 2013, A&A, 549, A45
Dodson, R. G., & Ellingsen, S. P. 2002, MNRAS, 333, 307
Doyle, K. B. 2009, SPIE Conf. Ser, 7427, 9
Faúndez, S., Bronfman, L., Garay, G., Chini, R., Nyman, L.-Å., & May, J. 2004, A&A, 426, 97
Foster, J. B., et al. 2011, ApJS, 197, 25
Franco-Hernández, R., & Rodríguez, L. F. 2004, ApJ, 604, L105
Galván-Madrid, R., Rodríguez, L. F., Ho, P. T. P., & Keto, E. 2008, ApJ, 674, L33
Galván-Madrid, R., Peters, T., Keto, E. R., Mac Low, M., Banerjee, R., & Klessen, R. 2011, MNRAS, 416, 1033
Green, J. A., et al. 2009, MNRAS, 392, 783
Gum, C. S. 1955, MmRAS, 67, 155
Haario, H., Saksman, E., & Tamminen, J. 1998, Bernoulli, 7, 223
Han, J. L., & Zhang, J. S. 2007, A&A, 464, 609
Jones, P. A., et al. 2012, MNRAS, 419, 2961
Klassen, M., Peters, T., & Pudritz, R. E. 2012, ApJ, 758, 137
Kwok, S., Volk, K., & Bidelman, W. P. 1997, ApJS, 112, 557
Ladd, N., Purcell, C., Wong, T., & Robertson, S. 2005, PASA, 22, 62
Peters, T., Klessen, R. S., Mac Low, M., & Banerjee, R. 2010, ApJ, 725, 134
Robinson, B. J., Caswell, J. L., & Goss, W. M. 1974, AuJPh, 27, 575
Rodgers, A. W., Campbell, C. T., & Whiteoak, J. B. 1960, MNRAS, 121, 103
Schuller, F., et al. 2009, A&A, 504, 415
Urquhart, J. S., et al. 2010, PASA, 27, 321
van Dishoeck, E. F., & Blake, G. A. 1998, ARA&A, 36, 317
Vilas-Boas, J. W. S., & Abraham, Z. 2000, A&A, 355, 1115
Viti, S., Collings, M. P., Dever, J. W., McCoustra, M. R. S., & Williams, D. A. 2004, MNRAS, 354, 1141
Walsh, A. J., Bertoldi, F., Burton, M. G., & Nikola, T. 2001, MNRAS, 326, 36
Walsh, A. J., Burton, M. G., Hyland, A. R., & Robinson, G. 1998, MNRAS, 301, 640
Walsh, A. J., Burton, M. G., Hyland, A. R., & Robinson, G. 1999, MNRAS, 309, 905
Zinchenko, I., Henkel, C., & Mao, R. Q. 2000, A&A, 361, 1079

APPENDIX: PSW OBSERVATIONS

Table A1 presents a summary of every PSW observation of G301, including the file number, the name of the file (which incorporates the UT date when the observation was started) and the parameters important in assessing pointing reliability and gain variations. These include the azimuth, elevation, the time (listed as modified Julian date or MJD), the time-of-day (hours since sunrise), the ambient temperature at the time of observations, and the time since May 1 within each observing season (our proxy for time-of-year).

Table A2 shows the fit parameters (velocity and amplitude) with uncertainty for the central components of each of the four main transitions. Parameters are only shown if the fit was reasonable according to the criteria given in equations (1)–(3). Our analysis excludes the data taken on the first day of the survey, 2010 September 11 (the date convention is YYYY-MM-DD), as it was observed in a different IF configuration. We also exclude data from 2012 September 3 when the paddle wheel was broken, resulting in a meaningless measurement of T_{sys} (9 999 K) in Table A2 and uncalibrated amplitudes.

Table A1. Properties of PSW observations of G301.

No.[a]	Name	T_{sys} (K)	Elevation (deg)	Azimuth (deg)	MJD (d)	Time of day[b] (h)	Temperature (°C)	Time since May 1 (10^7 s)
0	2010-07-12_1	432	40.08	146.79	55389.297	7.11	11.9	0.62321
1	2010-07-12_2	521	36.40	146.43	55389.276	6.59	11.6	0.62302
2	2010-07-12_3	496	37.44	146.47	55389.282	6.74	11.6	0.62307
3	2010-07-12_4	438	39.07	146.63	55389.291	6.96	11.9	0.62316
4	2010-07-13_1	303	39.18	146.65	55390.289	6.92	13.3	0.63178
5	2010-07-14_1	193	34.01	146.49	55391.256	6.13	9.5	0.64013
6	2010-07-15_1	184	35.57	146.42	55392.263	6.28	7.9	0.64883
7	2010-07-16_1	170	35.43	146.43	55393.259	6.21	9.3	0.65744
8	2010-07-17_1	169	34.89	146.44	55394.253	6.07	11.8	0.66603
9	2010-07-17_2	170	33.01	146.58	55394.242	5.81	11.8	0.66593
10	2010-07-17_3	170	33.95	146.50	55394.248	5.94	11.7	0.66598
11	2010-07-18_1	183	34.37	146.47	55395.247	5.94	14.0	0.67462
12	2010-07-18_2	187	33.37	146.55	55395.241	5.80	13.7	0.67457
13	2010-07-19_1	192	54.92	158.56	55396.377	9.07	12.6	0.68438
14	2010-07-20_1	153	58.15	− 167.99	55397.485	11.66	6.0	0.69395
15	2010-07-20_2	153	57.56	− 165.56	55397.493	11.86	5.6	0.69402
16	2010-07-26_1	190	42.19	147.29	55403.271	6.58	12.3	0.74395
17	2010-07-27_1	209	37.27	146.46	55404.240	5.83	12.9	0.75231
18	2010-07-29_1	546	56.07	− 161.10	55406.485	11.74	11.8	0.77171
19	2010-07-29_2	1730	56.10	161.16	55406.361	8.76	11.6	0.77064
20	2010-07-29_3	1595	56.63	162.57	55406.367	8.89	11.7	0.77069
21	2010-07-29_4	1425	57.13	164.07	55406.372	9.03	11.8	0.77074
22	2010-07-29_5	1107	57.57	165.60	55406.378	9.16	11.8	0.77078
23	2010-07-29_6	1119	58.04	167.51	55406.384	9.32	12.1	0.77084
24	2010-07-29_7	1437	58.40	169.26	55406.390	9.46	12.0	0.77089
25	2010-07-29_8	947	58.74	− 171.25	55406.450	10.89	11.8	0.77141
26	2010-07-30_1	1072	39.73	146.73	55407.246	6.00	12.2	0.77829
27	2010-07-31_1	327	38.22	146.53	55408.234	5.73	10.3	0.78682
28	2010-08-03_1	158	58.57	− 170.16	55411.440	10.7	9.5	0.81452
29	2010-08-04_1	165	37.40	146.47	55412.219	5.41	11.8	0.82125
30	2010-08-05_1	177	38.29	146.54	55413.221	5.48	9.7	0.82991
31	2010-08-06_1	165	36.96	146.44	55414.211	5.24	6.3	0.83846
32	2010-08-07_1	166	38.43	146.55	55415.216	5.40	9.4	0.84715
33	2010-08-08_1	165	39.15	146.64	55416.218	5.45	11.8	0.85580
34	2010-08-09_1	183	42.26	147.32	55417.234	5.85	14.3	0.86458
35	2010-08-10_1	9712	39.64	− 146.72	55418.565	13.83	11.5	0.87608
36	2010-08-11_1	249	38.08	146.52	55419.204	5.15	6.9	0.88160
37	2010-08-13_1	174	37.96	146.51	55421.197	5.03	7.8	0.89882
38	2010-08-14_1	164	38.47	146.56	55422.198	5.06	10.0	0.90747
39	2010-08-15_1	195	38.36	146.54	55423.194	4.99	11.2	0.91608
40	2010-08-16_1	179	38.87	146.60	55424.195	5.02	9.3	0.92472
41	2010-08-17_1	152	38.16	146.52	55425.188	4.87	7.1	0.93330
42	2010-08-18_1	214	37.93	146.50	55426.183	4.79	13.4	0.94191
43	2010-08-18_2	217	36.27	146.42	55426.174	4.56	12.8	0.94182
44	2010-08-19_1	942	41.28	147.05	55427.201	5.22	10.7	0.95069
45	2010-08-20_1	165	37.18	146.45	55428.174	4.59	8.9	0.95910
46	2010-08-21_1	165	37.46	146.47	55429.173	4.59	7.7	0.96773

Table A1. Continued

No.[a]	Name	T_{sys} (K)	Elevation (deg)	Azimuth (deg)	MJD (d)	Time of day[b] (h)	Temperature (°C)	Time since May 1 (10^7 s)
47	2010-08-22_1	159	37.79	146.49	55430.172	4.59	8.6	0.97636
48	2010-08-26_1	195	38.16	146.52	55435.160	4.41	7.1	1.01946
49	2010-08-26_2	265	39.43	146.68	55434.170	4.63	5.9	1.01091
50	2010-08-26_3	218	40.38	146.85	55434.176	4.77	6.1	1.01096
51	2010-08-26_4	269	58.69	– 170.89	55434.374	9.53	6.8	1.01267
52	2010-08-27_1	175	39.46	146.68	55436.165	4.55	7.1	1.02815
53	2010-08-29_1	193	39.83	146.75	55438.162	4.51	14.1	1.04540
54	2010-08-30_1	177	36.18	146.42	55439.138	3.95	13.1	1.05383
55	2010-08-30_2	177	44.40	148.09	55438.189	5.16	14.8	1.04564
56	2010-08-31_1	214	38.87	146.60	55440.151	4.28	12.9	1.06258
57	2010-08-31_2	159	55.39	159.52	55439.264	6.99	16.3	1.05492
58	2010-09-01_1	269	36.62	146.43	55441.135	3.92	17.8	1.07108
59	2010-09-02_1	308	37.19	146.45	55442.135	3.95	14.2	1.07973
60	2010-09-02_2	411	56.89	– 163.31	55441.381	9.83	21.9	1.07321
61	2010-09-07_1	169	42.62	147.42	55447.154	4.49	10.3	1.12309
62	2010-09-07_2	156	52.34	– 154.41	55446.408	10.57	9.9	1.11664
63	2010-09-08_1	323	40.15	146.80	55448.136	4.09	12.9	1.13158
64	2010-09-10_1	217	26.98	– 147.89	55449.556	14.17	9.1	1.14384
65	2010-09-10_2	182	53.86	156.64	55449.224	6.21	15.6	1.14097
66	2010-09-11_1	161	53.57	156.17	55450.219	6.10	11.9	1.14957
67	2010-09-12_1	165	54.75	158.21	55451.226	6.29	16.3	1.15827
68	2010-09-13_1	213	55.13	158.96	55452.226	6.32	16.4	1.16692
69	2010-09-14_1	331	55.07	158.84	55453.223	6.27	16.0	1.17553
70	2010-09-15_1	166	55.13	158.96	55454.221	6.23	11.0	1.18415
71	2010-09-16_1	192	55.66	160.12	55455.223	6.31	9.9	1.19281
72	2010-09-17_1	144	56.20	161.40	55456.226	6.39	8.6	1.20147
73	2010-09-18_1	156	58.19	168.16	55457.247	6.93	14.9	1.21030
74	2010-09-19_1	176	53.97	156.82	55458.200	5.82	10.8	1.21853
75	2010-09-20_1	217	54.76	158.23	55459.204	5.94	14.1	1.22720
76	2010-09-21_1	212	58.88	172.28	55460.252	7.12	18.3	1.23626
77	2010-09-21_2	219	54.19	157.18	55460.196	5.78	16.1	1.23578
78	2011-05-06_1	165	43.43	– 147.71	55687.806	19.7	7.7	0.04872
79	2011-05-07_1	174	42.73	– 147.47	55688.807	19.72	10.9	0.05737
80	2011-05-08_1	194	43.45	– 147.72	55689.800	19.54	9.3	0.06595
81	2011-05-23_1	246	41.97	– 147.24	55704.768	18.62	8.6	0.19528
82	2011-05-24_1	262	36.90	– 146.45	55705.795	19.26	6.1	0.20415
83	2011-05-25_1	231	26.32	– 148.13	55706.855	20.69	5.8	0.21331
84	2011-05-26_1	183	47.22	– 149.61	55707.728	17.62	6.6	0.22085
85	2011-05-27_1	147	39.87	146.76	55708.422	10.28	8.3	0.22685
86	2011-05-28_1	152	40.04	146.79	55709.421	10.23	11.7	0.23547
87	2011-05-29_1	176	38.87	146.61	55710.411	9.99	11.2	0.24403
88	2011-05-31_1	217	59.29	177.04	55712.576	13.94	9.1	0.26274
89	2011-06-06_1	157	46.38	149.10	55718.434	10.49	9.4	0.31335
90	2011-06-07_1	182	38.98	146.63	55719.387	9.35	9.6	0.32158
91	2011-06-27_1	174	37.95	146.51	55739.326	7.80	13.9	0.49386
92	2011-06-28_1	186	38.56	146.58	55740.327	7.81	14.4	0.50251
93	2011-06-29_1	158	54.62	157.99	55741.430	10.28	11.8	0.51204
94	2011-06-30_1	161	38.77	146.60	55742.323	7.71	12.7	0.51975
95	2011-07-19_1	173	58.84	171.96	55761.427	10.26	4.4	0.68481
96	2011-07-27_1	134	59.31	177.45	55769.422	10.2	9.9	0.75388
97	2011-07-28_1	152	37.88	146.51	55770.241	5.88	13.7	0.76097
98	2011-07-29_1	159	38.74	146.59	55771.244	5.94	14.8	0.76963
99	2011-07-30_1	170	39.25	146.66	55772.244	5.95	14.2	0.77827
100	2011-07-31_1	196	39.11	146.64	55773.240	5.87	16.0	0.78688
101	2011-08-01_1	180	39.85	146.76	55774.242	5.92	17.7	0.79553
102	2011-08-02_1	163	40.70	146.92	55775.244	5.99	18.7	0.80419
103	2011-08-03_1	191	37.53	146.48	55776.223	5.49	18.6	0.81265
104	2011-08-04_1	166	39.59	146.71	55777.232	5.73	18.4	0.82137
105	2011-08-05_1	178	38.38	146.55	55778.222	5.51	15.6	0.82992
106	2011-08-06_1	201	38.53	146.57	55779.221	5.48	15.7	0.83855
107	2011-08-07_1	247	38.92	146.62	55780.220	5.49	12.3	0.84718

Table A1. Continued

No.[a]	Name	T_{sys} (K)	Elevation (deg)	Azimuth (deg)	MJD (d)	Time of day[b] (h)	Temperature (°C)	Time since May 1 (10^7 s)
108	2011-08-08_1	181	39.24	146.66	55781.219	5.48	9.7	0.85581
109	2011-08-09_1	204	51.79	153.73	55782.296	7.34	5.7	0.86512
110	2011-08-10_1	184	40.27	146.83	55783.220	5.53	8.4	0.87310
111	2011-08-11_1	187	36.87	146.45	55784.197	5.00	7.9	0.88154
112	2011-08-16_1	187	57.38	− 164.91	55789.423	10.49	16.9	0.92669
113	2011-08-18_1	194	46.03	148.90	55791.233	5.98	7.6	0.94233
114	2011-08-19_1	572	37.80	146.50	55792.181	4.74	7.9	0.95052
115	2011-08-20_1	242	37.96	146.51	55793.179	4.72	9.8	0.95915
116	2011-08-21_1	176	38.78	146.60	55794.181	4.79	10.3	0.96780
117	2011-08-22_1	169	39.06	146.63	55795.180	4.79	10.2	0.97644
118	2011-08-23_1	146	40.79	146.94	55796.188	4.99	11.7	0.98514
119	2011-08-23_2	149	39.89	146.76	55796.182	4.86	11.5	0.98509
120	2011-08-24_1	145	40.52	146.88	55797.183	4.90	15.3	0.99374
121	2011-08-24_2	143	39.60	146.71	55797.178	4.77	14.5	0.99370
122	2011-08-25_1	145	40.38	146.85	55798.180	4.83	16.6	1.00235
123	2011-08-26_1	150	40.85	146.95	55799.180	4.85	16.2	1.01099
124	2011-08-26_2	377	37.77	146.50	55800.159	4.37	13.4	1.01945
125	2011-08-27_1	180	37.76	146.50	55801.156	4.33	18.3	1.02807
126	2011-08-28_1	185	39.07	146.64	55802.161	4.46	16.6	1.03675
127	2011-08-30_1	156	47.13	149.55	55803.207	5.59	18.5	1.04579
128	2011-08-30_2	167	37.18	146.46	55804.144	4.11	14.1	1.05389
129	2011-08-31_1	161	37.34	146.47	55805.143	4.08	15.7	1.06251
130	2011-09-01_1	182	39.13	146.64	55806.150	4.29	12.6	1.07122
131	2011-09-01_2	183	38.21	146.53	55806.145	4.16	12.2	1.07117
132	2011-09-02_1	177	38.65	146.58	55807.145	4.17	13.8	1.07981
133	2011-09-03_1	172	38.13	146.53	55808.139	4.06	13.3	1.08840
134	2011-09-04_1	175	40.31	146.84	55809.149	4.32	15.0	1.09713
135	2011-09-07_1	200	39.63	− 146.72	55811.490	12.54	16.2	1.11735
136	2011-09-09_1	185	37.73	− 146.49	55813.495	12.71	6.5	1.13468
137	2011-09-10_1	161	37.52	− 146.48	55814.494	12.69	7.8	1.14331
138	2011-09-11_1	226	36.22	− 146.43	55815.499	12.83	6.5	1.15199
139	2011-09-12_1	174	36.46	− 146.43	55816.495	12.75	9.5	1.16059
140	2011-09-13_1	134	55.85	− 160.56	55817.363	9.60	16.8	1.16809
141	2011-09-13_2	144	38.72	146.59	55818.115	3.67	13.9	1.17460
142	2011-09-14_1	167	40.30	146.84	55819.122	3.85	18.7	1.18329
143	2011-09-15_1	177	38.68	146.58	55820.109	3.58	18.5	1.19183
144	2011-09-15_2	177	37.77	146.49	55820.104	3.45	18.3	1.19178
145	2011-09-16_1	176	35.76	146.42	55821.090	3.12	21.7	1.20029
146	2011-09-17_1	157	37.49	146.47	55822.097	3.32	21.7	1.20900
147	2011-09-18_1	176	36.01	146.42	55823.086	3.07	19.7	1.21754
148	2011-09-26_1	179	50.49	152.28	55831.153	4.87	16.3	1.28724
149	2011-09-28_1	216	53.05	155.38	55832.169	5.28	14.9	1.29602
150	2011-10-14_1	221	50.52	− 152.30	55848.321	9.24	21.7	1.43557
151	2011-10-14_2	220	51.30	− 153.14	55848.315	9.11	21.5	1.43552
152	2012-06-27_1	231	59.35	178.82	56105.506	12.1	8.4	0.49541
153	2012-06-29_1	191	56.63	162.61	56107.448	10.7	12.3	0.51219
154	2012-06-30_1	173	54.35	157.50	56108.423	10.11	12.4	0.52062
155	2012-07-01_1	188	54.84	158.43	56109.425	10.14	8.3	0.52927
156	2012-07-02_1	171	54.33	157.48	56110.418	9.97	5.4	0.53785
157	2012-07-03_1	160	55.52	159.82	56111.425	10.16	7.2	0.54656
158	2012-07-04_1	158	55.15	159.04	56112.419	10.02	7.9	0.55514
159	2012-07-05_1	164	55.69	160.21	56113.421	10.07	8.7	0.56380
160	2012-07-06_1	183	56.50	162.24	56114.427	10.21	9.9	0.57249
161	2012-07-07_1	162	55.44	159.66	56115.414	9.89	11.3	0.58101
162	2012-07-08_1	169	55.27	159.29	56116.409	9.79	12.7	0.58962
163	2012-07-23_1	193	58.32	168.89	56131.404	9.74	9.9	0.71917
164	2012-07-23_2	173	57.50	165.39	56131.392	9.46	9.8	0.71907
165	2012-07-24_1	166	56.94	163.51	56132.383	9.24	12.3	0.72763
166	2012-07-25_1	192	57.35	164.86	56133.385	9.30	13.2	0.73628
167	2012-07-26_1	186	58.17	168.14	56134.393	9.51	13.7	0.74500

Table A1. Continued

No.[a]	Name	T_{sys} (K)	Elevation (deg)	Azimuth (deg)	MJD (d)	Time of day[b] (h)	Temperature (°C)	Time since May 1 (10^7 s)
168	2012-07-27_1	182	56.42	162.02	56135.369	8.93	8.8	0.75343
169	2012-07-28_1	173	59.24	− 176.16	56136.436	10.55	6.7	0.76265
170	2012-07-29_1	173	56.64	162.62	56137.366	8.87	8.6	0.77068
171	2012-07-30_1	150	56.87	163.30	56138.365	8.87	9.3	0.77932
172	2012-07-31_1	161	56.77	163.01	56139.362	8.79	10.2	0.78792
173	2012-08-01_1	170	56.67	162.71	56140.358	8.70	8.6	0.79653
174	2012-08-02_1	158	57.17	164.24	56141.361	8.79	12.3	0.80520
175	2012-08-03_1	167	55.38	159.53	56142.339	8.29	12.3	0.81365
176	2012-08-04_1	165	56.00	160.94	56143.343	8.38	13.7	0.82232
177	2012-08-05_1	170	55.94	160.81	56144.339	8.32	14.8	0.83093
178	2012-08-06_1	151	56.56	162.41	56145.343	8.42	9.9	0.83960
179	2012-08-07_1	164	56.54	162.34	56146.340	8.37	13.1	0.84822
180	2012-08-08_1	154	56.79	163.05	56147.340	8.38	15.2	0.85686
181	2012-08-10_1	155	58.80	171.76	56149.364	8.99	7.5	0.87435
182	2012-08-11_1	161	57.55	165.57	56150.341	8.45	10.9	0.88279
183	2012-08-12_1	164	56.41	162.00	56151.325	8.08	11.9	0.89129
184	2012-08-13_1	171	56.37	161.89	56152.322	8.02	13.4	0.89990
185	2012-08-14_1	152	55.82	160.52	56153.314	7.84	15.4	0.90847
186	2012-08-15_1	168	57.43	165.13	56154.328	8.21	17.3	0.91724
187	2012-08-16_1	165	57.65	165.95	56155.329	8.24	15.1	0.92588
188	2012-08-17_1	174	59.29	177.11	56156.361	9.04	10.8	0.93480
189	2012-08-18_1	323	56.67	162.70	56157.311	7.86	7.4	0.94301
190	2012-08-19_1	161	56.24	161.56	56158.304	7.71	12.7	0.95159
191	2012-08-20_1	151	56.41	161.98	56159.303	7.70	14.1	0.96022
192	2012-08-21_1	185	56.61	162.53	56160.302	7.71	18.4	0.96885
193	2012-08-22_1	206	56.89	163.37	56161.303	7.74	17.3	0.97750
194	2012-08-24_1	150	58.73	171.23	56163.324	8.29	14.7	0.99496
195	2012-08-25_1	169	57.89	166.87	56164.307	7.90	14.7	1.00345
196	2012-08-26_1	160	56.19	161.41	56165.284	7.37	11.2	1.01190
197	2012-08-27_1	158	56.65	162.65	56166.287	7.44	13.0	1.02056
198	2012-08-28_1	163	56.81	163.13	56167.286	7.44	16.3	1.02919
199	2012-08-29_1	183	57.09	163.99	56168.286	7.47	18.4	1.03783
200	2012-08-30_1	162	57.04	163.83	56169.283	7.41	14.2	1.04644
201	2012-08-31_1	153	57.56	165.60	56170.286	7.52	9.6	1.05511
202	2012-09-01_1	149	57.62	165.82	56171.285	7.49	9.9	1.06374
203	2012-09-01_2	146	59.36	− 179.65	56171.330	8.59	10.1	1.06413
204	2012-09-02_1	153	55.44	159.65	56172.258	6.88	14.3	1.07215
205	2012-09-03_1	9999	50.76	− 152.57	56173.429	11.0	16.0	1.08227
206	2012-09-04_1	165	56.20	161.43	56174.260	6.96	19.8	1.08945
207	2012-09-05_1	164	57.20	164.34	56175.268	7.18	19.8	1.09816
208	2012-09-06_1	162	57.74	166.28	56176.272	7.30	20.4	1.10683
209	2012-09-07_1	178	58.55	170.12	56177.282	7.56	15.6	1.11556
210	2012-09-08_1	168	57.22	164.38	56178.260	7.04	12.5	1.12401
211	2012-09-09_1	212	57.12	164.06	56179.256	6.97	13.4	1.13261
212	2012-09-09_2	159	57.57	165.62	56179.262	7.10	13.4	1.13266
213	2012-09-10_1	161	55.70	160.23	56180.239	6.56	18.2	1.14110
214	2012-09-11_1	178	55.77	160.38	56181.237	6.53	20.6	1.14972
215	2012-09-12_1	151	56.20	161.44	56182.238	6.59	21.7	1.15838
216	2012-09-13_1	234	58.47	169.64	56183.265	7.24	19.2	1.16725
217	2012-09-14_1	153	57.81	166.57	56184.252	6.95	11.2	1.17577
218	2012-09-17_1	191	55.55	159.88	56187.218	6.21	19.7	1.20140
219	2012-09-19_1	165	55.63	160.07	56189.213	6.14	16.7	1.21864
220	2012-09-20_1	195	55.42	159.60	56190.209	6.05	22.5	1.22724
221	2012-09-21_1	221	56.75	162.93	56191.219	6.33	18.8	1.23597
222	2012-09-22_1	156	57.17	164.25	56192.221	6.40	16.9	1.24463
223	2012-09-23_1	182	55.87	160.63	56193.205	6.03	22.9	1.25313
224	2012-09-30_1	149	59.07	173.96	56200.232	6.83	12.0	1.31384
225	2012-10-01_1	159	58.14	167.99	56201.210	6.33	15.5	1.32229
226	2012-10-02_1	163	58.61	170.49	56202.215	6.48	15.4	1.33098
227	2012-10-03_1	164	59.17	− 175.14	56203.256	7.48	20.8	1.33997
228	2012-10-04_1	163	56.85	163.21	56204.185	5.79	22.7	1.34800

Table A1. Continued

No.[a]	Name	T_{sys} (K)	Elevation (deg)	Azimuth (deg)	MJD (d)	Time of day[b] (h)	Temperature (°C)	Time since May 1 (10^7 s)
229	2012-10-05_1	184	56.81	163.11	56205.182	5.74	26.0	1.35661
230	2012-10-06_1	177	56.79	163.06	56206.179	5.68	27.1	1.36523
231	2012-10-07_1	143	57.66	165.95	56207.187	5.89	13.3	1.37393
232	2012-10-08_1	158	56.91	163.40	56208.175	5.62	16.0	1.38247
233	2012-10-10_1	179	57.07	163.90	56210.171	5.57	20.6	1.39972
234	2012-10-11_1	171	59.20	175.49	56211.206	6.44	10.6	1.40866
235	2012-10-12_1	200	45.78	− 148.77	56212.355	10.03	9.5	1.41859
236	2012-10-13_1	167	57.05	163.84	56214.160	5.38	13.7	1.43418
237	2012-10-14_1	166	57.25	164.49	56215.160	5.39	18.7	1.44282
238	2012-10-15_1	175	57.22	164.39	56216.157	5.34	21.4	1.45143
239	2012-10-16_1	174	57.53	165.45	56217.158	5.38	25.1	1.46008
240	2012-10-17_1	160	57.72	166.20	56218.158	5.40	21.0	1.46872
241	2012-10-18_1	224	55.97	160.86	56219.135	4.87	23.2	1.47716
242	2012-10-19_1	150	56.24	161.54	56220.135	4.89	26.1	1.48580
243	2012-10-21_1	211	59.36	− 179.23	56221.195	6.35	23.1	1.49496
244	2012-10-28_1	219	56.84	163.18	56229.117	4.61	16.6	1.56341
245	2012-10-30_1	206	57.73	166.21	56231.122	4.77	23.3	1.58073

[a]Sequential numbering of PSW observations.
[b]Time of day is calculated as the numbers of hours since sunrise.

Table A2. Fit results for PSW observations of G301.

	Parameters of Gaussian fits to transitions[a]								Best-fit locations[b]	
	N_2H^+		HNC		HCO^+		HCN			
No	$\langle a \rangle$ (K)	$\langle v \rangle$ (km s^{-1})	$\langle a \rangle$ (K)	$\langle v \rangle$ (km s^{-1})	$\langle a \rangle$ (K)	$\langle v \rangle$ (km s^{-1})	$\langle a \rangle$ (K)	$\langle v \rangle$ (km s^{-1})	l (deg)	b (deg)
4	1.07(5)	− 42.53(6)	2.01(4)	− 42.80(4)	3.32(4)	− 42.70(3)	2.46(6)	− 43.01(6)	300.9678	+1.1446
5	0.87(3)	− 42.49(5)	1.60(3)	− 42.79(3)	2.63(3)	− 42.68(2)	2.12(3)	− 42.98(4)	300.9672	+1.1440
6	1.01(3)	− 42.41(4)	1.78(3)	− 42.74(3)	2.87(3)	− 42.62(2)	2.27(3)	− 42.91(4)	300.9753	+1.1446
7	1.16(3)	− 42.37(3)	1.87(2)	− 42.65(2)	2.99(2)	− 42.59(2)	2.35(3)	− 42.85(3)	300.9772	+1.1440
8	1.98(3)	− 42.53(2)	2.57(3)	− 42.75(2)	3.93(3)	− 42.68(1)	2.84(3)	− 42.83(2)	300.9659	+1.1434
9	1.65(3)	− 42.51(2)	2.36(2)	− 42.77(2)	3.82(3)	− 42.68(1)	2.64(3)	− 42.97(3)	300.9678	+1.1440
10	1.91(3)	− 42.60(2)	2.53(3)	− 42.76(2)	3.94(3)	− 42.69(1)	2.81(3)	− 42.84(2)	300.9666	+1.1434
12	1.08(3)	− 42.39(4)	1.97(3)	− 42.79(2)	3.27(3)	− 42.69(2)	2.46(3)	− 43.05(3)	300.9722	+1.1465
13	1.57(3)	− 42.46(3)	2.36(3)	− 42.72(2)	3.74(3)	− 42.63(1)	2.81(3)	− 42.94(3)	300.9678	+1.1428
14	2.05(3)	− 42.59(2)	2.76(2)	− 42.77(1)	4.09(2)	− 42.70(1)	2.94(3)	− 42.86(2)	300.9672	+1.1434
16	1.01(3)	− 42.45(4)	1.80(3)	− 42.62(3)	2.83(3)	− 42.59(2)	2.21(3)	− 42.88(4)	300.9747	+1.1434
17	1.33(3)	− 42.50(4)	1.97(3)	− 42.66(3)	3.02(3)	− 42.58(2)	2.37(4)	− 42.80(4)	300.9659	+1.1415
27	1.31(5)	− 42.59(5)	2.25(4)	− 42.72(3)	3.46(4)	− 42.72(2)	2.57(6)	− 43.07(5)	300.9691	+1.1446
28	1.98(3)	− 42.59(2)	2.51(2)	− 42.73(1)	3.50(2)	− 42.63(1)	2.80(3)	− 42.79(2)	300.9684	+1.1409
29	0.96(3)	− 42.37(4)	1.65(2)	− 42.67(2)	2.52(2)	− 42.58(2)	2.12(3)	− 42.84(3)	300.9772	+1.1440
30	0.85(3)	− 42.41(5)	1.62(3)	− 42.73(3)	2.65(2)	− 42.66(2)	2.12(3)	− 42.99(4)	300.9734	+1.1453
31	1.41(3)	− 42.47(3)	2.20(2)	− 42.70(2)	3.32(2)	− 42.64(1)	2.54(3)	− 42.90(3)	300.9666	+1.1428
32	0.91(3)	− 42.45(4)	1.72(2)	− 42.65(2)	2.70(2)	− 42.58(2)	2.14(3)	− 42.92(4)	300.9741	+1.1434
33	1.13(3)	− 42.41(3)	2.11(2)	− 42.80(2)	3.30(2)	− 42.67(1)	2.53(3)	− 43.07(3)	300.9716	+1.1465
34	1.10(3)	− 42.37(4)	1.79(3)	− 42.69(3)	2.79(2)	− 42.59(2)	2.26(3)	− 42.90(4)	300.9760	+1.1440
36	1.20(4)	− 42.56(4)	1.78(3)	− 42.71(3)	2.54(3)	− 42.63(2)	2.12(4)	− 42.83(4)	300.9672	+1.1421
37	1.63(3)	− 42.56(2)	2.37(2)	− 42.78(2)	3.72(3)	− 42.67(1)	2.66(3)	− 42.95(3)	300.9678	+1.1440
38	1.18(3)	− 42.47(3)	1.97(2)	− 42.75(2)	2.78(3)	− 42.70(2)	2.38(3)	− 43.01(3)	300.9728	+1.1459
39	0.97(3)	− 42.49(5)	1.85(3)	− 42.76(3)	3.10(3)	− 42.74(2)	2.33(3)	− 43.02(4)	300.9672	+1.1446
40	1.08(3)	− 42.44(4)	2.01(2)	− 42.82(2)	3.37(3)	− 42.70(2)	2.50(3)	− 43.08(3)	300.9709	+1.1465
41	1.59(2)	− 42.55(2)	2.25(2)	− 42.72(2)	3.57(2)	− 42.67(1)	2.54(3)	− 42.96(3)	300.9684	+1.1434
42	1.26(4)	− 42.58(4)	2.03(3)	− 42.84(3)	3.33(3)	− 42.76(2)	2.40(3)	− 42.98(4)	300.9666	+1.1453
43	1.08(3)	− 42.45(4)	1.89(3)	− 42.78(3)	3.02(3)	− 42.66(2)	2.23(4)	− 42.96(5)	300.9672	+1.1440
45	1.48(3)	− 42.56(2)	2.05(2)	− 42.70(2)	3.17(2)	− 42.65(1)	2.39(3)	− 42.89(3)	300.9678	+1.1428

Table A2. Continued

	Parameters of Gaussian fits to transitions[a]								Best-fit locations[b]	
	N_2H^+		HNC		HCO^+		HCN			
No.	$\langle a \rangle$ (K)	$\langle v \rangle$ (km s^{-1})	$\langle a \rangle$ (K)	$\langle v \rangle$ (km s^{-1})	$\langle a \rangle$ (K)	$\langle v \rangle$ (km s^{-1})	$\langle a \rangle$ (K)	$\langle v \rangle$ (km s^{-1})	l (deg)	b (deg)
46	1.41(3)	− 42.53(3)	2.10(2)	− 42.73(2)	3.32(2)	− 42.63(1)	2.42(3)	− 42.88(3)	300.9672	+1.1428
47	1.37(3)	− 42.57(2)	2.11(2)	− 42.74(2)	3.29(2)	− 42.65(1)	2.44(3)	− 42.91(3)	300.9684	+1.1428
48	1.13(3)	− 42.52(4)	1.98(3)	− 42.73(2)	3.02(3)	− 42.69(2)	2.25(4)	− 42.99(4)	300.9678	+1.1440
49	0.89(4)	− 42.46(6)	1.83(4)	− 42.81(3)	2.93(4)	− 42.76(2)	2.34(4)	− 43.09(5)	300.9716	+1.1478
50	1.11(4)	− 42.52(4)	1.98(3)	− 42.79(3)	3.20(3)	− 42.69(2)	2.36(4)	− 43.00(4)	300.9678	+1.1446
51	1.64(5)	− 42.62(4)	2.28(4)	− 42.83(3)	3.50(4)	− 42.74(2)	2.57(4)	− 42.90(4)	300.9659	+1.1453
52	1.10(3)	− 42.46(4)	1.90(2)	− 42.75(2)	3.09(2)	− 42.68(2)	2.32(3)	− 42.94(3)	300.9659	+1.1440
53	0.85(3)	− 42.47(5)	1.54(3)	− 42.71(3)	2.51(3)	− 42.66(2)	1.96(3)	− 42.94(5)	300.9672	+1.1434
54	1.09(3)	− 42.48(3)	1.62(3)	− 42.67(3)	2.55(2)	− 42.61(2)	2.04(3)	− 42.87(4)	300.9666	+1.1421
55	1.10(3)	− 42.51(3)	1.81(3)	− 42.74(2)	2.96(3)	− 42.70(2)	2.21(3)	− 42.90(3)	300.9659	+1.1440
56	1.10(3)	− 42.46(4)	1.90(3)	− 42.77(3)	3.21(3)	− 42.70(2)	2.24(4)	− 43.02(4)	300.9722	+1.1459
57	1.36(3)	− 42.52(3)	1.91(2)	− 42.67(2)	2.88(2)	− 42.59(1)	2.23(3)	− 42.84(3)	300.9672	+1.1415
58	1.22(5)	− 42.59(5)	1.77(4)	− 42.68(4)	2.63(4)	− 42.61(3)	2.19(5)	− 42.74(4)	300.9678	+1.1403
59	1.56(5)	− 42.58(5)	2.26(5)	− 42.72(3)	3.45(4)	− 42.65(2)	2.60(5)	− 42.92(4)	300.9684	+1.1428
61	1.16(3)	− 42.48(3)	2.08(2)	− 42.79(2)	3.45(2)	− 42.69(1)	2.56(3)	− 43.05(3)	300.9709	+1.1459
63	1.12(5)	− 42.48(6)	1.82(5)	− 42.71(5)	2.95(4)	− 42.66(3)	2.34(5)	− 43.01(6)	300.9697	+1.1440
64	1.57(4)	− 42.54(3)	2.17(3)	− 42.70(2)	3.50(3)	− 42.67(2)	2.45(3)	− 42.82(4)	300.9659	+1.1428
66	1.58(3)	− 42.49(2)	2.19(2)	− 42.71(2)	3.41(2)	− 42.65(1)	2.53(3)	− 42.94(3)	300.9678	+1.1434
67	1.40(3)	− 42.53(3)	2.00(2)	− 42.65(2)	3.00(2)	− 42.60(2)	2.35(3)	− 42.83(3)	300.9672	+1.1415
69	1.38(5)	− 42.46(5)	1.98(4)	− 42.63(4)	3.04(4)	− 42.53(3)	2.26(5)	− 42.80(5)	300.9659	+1.1409
70	1.46(3)	− 42.53(3)	2.08(2)	− 42.70(2)	3.21(2)	− 42.64(1)	2.44(3)	− 42.90(3)	300.9678	+1.1428
71	1.73(3)	− 42.54(2)	2.21(3)	− 42.68(2)	3.30(3)	− 42.64(2)	2.53(3)	− 42.85(3)	300.9672	+1.1421
72	1.66(2)	− 42.47(2)	2.36(2)	− 42.70(2)	3.58(2)	− 42.63(1)	2.56(3)	− 42.94(2)	300.9703	+1.1434
73	1.43(2)	− 42.49(2)	2.07(2)	− 42.70(2)	3.35(2)	− 42.64(1)	2.34(3)	− 42.83(3)	300.9659	+1.1428
74	1.44(3)	− 42.53(3)	1.99(3)	− 42.66(2)	2.96(3)	− 42.52(2)	2.36(3)	− 42.81(3)	300.9722	+1.1415
75	1.44(4)	− 42.53(3)	2.31(3)	− 42.76(2)	3.60(3)	− 42.72(2)	2.60(4)	− 42.94(3)	300.9666	+1.1440
76	1.44(3)	− 42.45(3)	2.20(3)	− 42.68(2)	3.35(3)	− 42.56(2)	2.58(4)	− 42.90(4)	300.9722	+1.1428
78	1.68(3)	− 42.52(2)	2.52(2)	− 42.81(2)	4.07(2)	− 42.69(1)	2.71(3)	− 42.93(3)	300.9666	+1.1440
79	1.22(3)	− 42.41(3)	1.81(3)	− 42.53(2)	2.78(3)	− 42.47(2)	2.02(3)	− 42.48(3)	300.9622	+1.1403
80	1.37(3)	− 42.43(3)	2.43(3)	− 42.78(2)	4.02(3)	− 42.72(1)	2.83(3)	− 43.03(3)	300.9734	+1.1465
81	1.68(4)	− 42.48(3)	2.31(4)	− 42.62(2)	3.42(4)	− 42.56(2)	2.35(4)	− 42.64(3)	300.9647	+1.1409
82	1.61(4)	− 42.48(4)	2.46(4)	− 42.77(3)	4.05(4)	− 42.64(2)	2.80(4)	− 42.95(4)	300.9678	+1.1434
83	1.54(4)	− 42.51(3)	2.21(3)	− 42.64(3)	3.41(3)	− 42.57(2)	2.49(3)	− 42.85(4)	300.9722	+1.1421
84	2.11(3)	− 42.55(2)	2.74(3)	− 42.71(2)	4.04(3)	− 42.65(1)	2.90(3)	− 42.84(2)	300.9672	+1.1421
85	1.02(2)	− 42.43(3)	1.83(2)	− 42.75(2)	3.03(2)	− 42.66(1)	2.21(3)	− 43.02(3)	300.9728	+1.1453
86	1.26(2)	− 42.45(3)	1.96(2)	− 42.81(2)	3.19(2)	− 42.70(1)	2.29(3)	− 42.99(3)	300.9666	+1.1446
87	0.88(3)	− 42.45(5)	1.61(2)	− 42.76(3)	2.69(2)	− 42.67(2)	2.07(3)	− 42.99(4)	300.9678	+1.1440
88	1.50(4)	− 42.59(3)	2.24(3)	− 42.88(2)	3.67(3)	− 42.77(2)	2.47(4)	− 43.05(3)	300.9678	+1.1459
89	1.58(2)	− 42.47(2)	2.27(2)	− 42.79(2)	3.60(2)	− 42.66(1)	2.57(3)	− 42.96(3)	300.9672	+1.1440
90	0.94(3)	− 42.46(5)	1.70(2)	− 42.78(3)	2.77(3)	− 42.73(2)	2.16(3)	− 43.03(4)	300.9672	+1.1446
91	0.70(3)	− 42.35(5)	1.49(2)	− 42.72(3)	2.42(2)	− 42.72(2)	2.01(3)	− 43.03(4)	300.9753	+1.1459
92	0.94(3)	− 42.43(5)	1.81(3)	− 42.69(3)	2.89(3)	− 42.65(2)	2.26(3)	− 42.99(4)	300.9734	+1.1446
93	1.48(3)	− 42.62(2)	1.97(2)	− 42.62(2)	2.82(2)	− 42.56(1)	2.19(3)	− 42.65(2)	300.9678	+1.1390
94	1.08(3)	− 42.42(3)	1.80(2)	− 42.73(2)	2.92(2)	− 42.66(2)	2.29(3)	− 42.94(3)	300.9741	+1.1453
95	1.55(3)	− 42.59(2)	2.21(3)	− 42.75(2)	3.35(3)	− 42.69(1)	2.47(3)	− 42.90(3)	300.9672	+1.1434
97	1.09(2)	− 42.47(3)	1.81(2)	− 42.71(2)	2.84(2)	− 42.63(2)	2.19(3)	− 42.96(3)	300.9728	+1.1446
98	0.93(2)	− 42.40(4)	1.58(2)	− 42.74(3)	2.59(2)	− 42.66(2)	2.04(2)	− 42.90(3)	300.9778	+1.1453
99	0.93(3)	− 42.43(4)	1.63(2)	− 42.70(3)	2.73(2)	− 42.68(2)	2.17(3)	− 42.96(3)	300.9747	+1.1453
100	0.90(3)	− 42.44(5)	1.72(3)	− 42.84(3)	2.96(3)	− 42.73(2)	2.22(3)	− 42.99(4)	300.9666	+1.1453
101	1.28(3)	− 42.50(3)	1.97(2)	− 42.69(2)	3.19(3)	− 42.64(2)	2.35(3)	− 42.95(3)	300.9703	+1.1434
102	1.09(3)	− 42.45(3)	1.85(2)	− 42.77(2)	2.97(2)	− 42.63(2)	2.31(3)	− 42.90(3)	300.9666	+1.1428
103	0.96(3)	− 42.49(5)	1.61(3)	− 42.64(3)	2.65(3)	− 42.65(2)	2.14(3)	− 42.91(4)	300.9678	+1.1421
104	1.16(3)	− 42.41(3)	1.80(2)	− 42.69(2)	2.81(2)	− 42.64(2)	2.18(3)	− 42.86(3)	300.9778	+1.1446
106	0.69(3)	− 42.42(7)	1.49(3)	− 42.73(3)	2.36(3)	− 42.70(2)	1.92(3)	− 42.90(5)	300.9659	+1.1440
108	0.78(3)	− 42.49(5)	1.42(3)	− 42.77(3)	2.35(2)	− 42.64(2)	1.93(3)	− 42.97(4)	300.9684	+1.1440
109	1.77(3)	− 42.55(2)	2.33(3)	− 42.74(2)	3.48(3)	− 42.67(2)	2.60(3)	− 42.85(3)	300.9672	+1.1428
110	0.92(3)	− 42.44(4)	1.47(3)	− 42.73(3)	2.32(2)	− 42.64(2)	1.97(3)	− 42.86(4)	300.9659	+1.1428

Table A2. Continued

	Parameters of Gaussian fits to transitions[a]								Best-fit locations[b]	
	N_2H^+		HNC		HCO^+		HCN			
No.	$\langle a \rangle$ (K)	$\langle v \rangle$ (km s^{-1})	$\langle a \rangle$ (K)	$\langle v \rangle$ (km s^{-1})	$\langle a \rangle$ (K)	$\langle v \rangle$ (km s^{-1})	$\langle a \rangle$ (K)	$\langle v \rangle$ (km s^{-1})	l (deg)	b (deg)
111	1.20(3)	− 42.45(3)	1.91(3)	− 42.73(2)	3.03(3)	− 42.64(2)	2.23(3)	− 42.94(4)	300.9734	+1.1446
112	0.91(3)	− 42.54(5)	1.83(3)	− 42.93(3)	3.33(3)	− 42.85(2)	2.34(4)	− 43.15(3)	300.9666	+1.1478
113	0.92(3)	− 42.55(5)	1.36(3)	− 42.69(3)	2.19(3)	− 42.52(3)	1.78(3)	− 42.83(5)	300.9709	+1.1415
116	1.04(3)	− 42.52(4)	1.89(2)	− 42.80(2)	3.19(2)	− 42.72(2)	2.26(3)	− 43.09(3)	300.9691	+1.1453
117	1.41(3)	− 42.57(3)	1.98(2)	− 42.75(2)	3.21(3)	− 42.68(1)	2.24(3)	− 42.87(3)	300.9672	+1.1434
118	1.40(2)	− 42.51(2)	1.99(2)	− 42.76(2)	3.13(2)	− 42.67(1)	2.23(2)	− 42.90(3)	300.9666	+1.1434
119	1.34(2)	− 42.58(2)	1.94(2)	− 42.73(2)	3.03(2)	− 42.65(1)	2.28(2)	− 42.86(2)	300.9678	+1.1428
121	1.03(2)	− 42.53(3)	1.77(2)	− 42.80(2)	3.01(2)	− 42.67(1)	2.16(2)	− 42.98(3)	300.9678	+1.1446
122	1.12(2)	− 42.55(3)	1.82(2)	− 42.74(2)	2.98(2)	− 42.68(1)	2.10(2)	− 42.93(3)	300.9672	+1.1434
123	1.32(2)	− 42.46(2)	1.95(2)	− 42.75(2)	3.18(2)	− 42.68(1)	2.25(3)	− 42.93(3)	300.9659	+1.1440
126	0.98(3)	− 42.53(4)	1.65(3)	− 42.75(3)	2.75(3)	− 42.64(2)	2.03(3)	− 42.94(4)	300.9678	+1.1434
127	1.10(3)	− 42.54(3)	1.98(2)	− 42.87(2)	3.29(2)	− 42.80(1)	2.27(3)	− 43.02(3)	300.9659	+1.1465
128	1.42(3)	− 42.49(3)	1.99(2)	− 42.74(2)	3.15(2)	− 42.64(1)	2.26(3)	− 42.86(3)	300.9666	+1.1428
129	1.02(3)	− 42.49(4)	1.68(2)	− 42.75(2)	2.52(2)	− 42.66(2)	1.88(3)	− 42.93(4)	300.9672	+1.1434
130	0.90(3)	− 42.48(4)	1.64(2)	− 42.81(3)	2.74(3)	− 42.76(2)	2.01(3)	− 43.08(4)	300.9716	+1.1478
132	0.87(3)	− 42.49(5)	1.64(2)	− 42.81(3)	2.73(4)	− 42.70(3)	2.01(3)	− 43.08(4)	300.9697	+1.1453
133	1.15(3)	− 42.51(3)	1.76(2)	− 42.74(2)	2.91(3)	− 42.67(2)	1.93(3)	− 42.90(4)	300.9666	+1.1434
135	1.27(3)	− 42.60(3)	2.05(3)	− 42.86(2)	3.38(3)	− 42.76(2)	2.32(3)	− 43.03(4)	300.9678	+1.1459
136	0.92(3)	− 42.43(4)	1.74(3)	− 42.85(3)	3.10(3)	− 42.79(2)	2.11(3)	− 43.09(4)	300.9716	+1.1484
137	0.72(3)	− 42.17(4)	1.16(3)	− 42.24(3)	1.98(3)	− 42.38(2)	1.27(3)	− 42.38(4)	300.9597	+1.1365
139	1.21(3)	− 42.53(3)	1.69(3)	− 42.57(2)	2.56(3)	− 42.52(2)	1.92(3)	− 42.63(3)	300.9653	+1.1390
141	1.00(2)	− 42.51(3)	1.79(2)	− 42.81(2)	3.09(2)	− 42.75(1)	2.11(3)	− 43.02(3)	300.9672	+1.1453
142	1.04(3)	− 42.50(4)	1.65(2)	− 42.74(2)	2.37(5)	− 42.63(4)	2.02(3)	− 42.89(3)	300.9666	+1.1428
143	0.97(3)	− 42.56(4)	1.78(2)	− 42.83(2)	2.92(2)	− 42.71(2)	2.11(3)	− 43.05(4)	300.9684	+1.1453
144	1.16(3)	− 42.50(3)	1.92(3)	− 42.76(2)	3.09(3)	− 42.66(2)	2.12(4)	− 42.98(4)	300.9684	+1.1440
145	1.00(3)	− 42.38(4)	1.68(2)	− 42.81(3)	2.77(2)	− 42.67(2)	2.06(3)	− 43.02(4)	300.9722	+1.1465
146	1.18(2)	− 42.50(3)	1.88(2)	− 42.76(2)	3.06(2)	− 42.72(1)	2.12(3)	− 42.98(3)	300.9672	+1.1446
147	1.04(3)	− 42.48(4)	1.68(2)	− 42.77(3)	2.73(2)	− 42.65(2)	2.15(3)	− 42.93(4)	300.9672	+1.1434
148	1.59(3)	− 42.55(2)	2.05(3)	− 42.70(2)	3.13(3)	− 42.67(2)	2.30(3)	− 42.86(3)	300.9672	+1.1428
150	1.41(4)	− 42.49(3)	1.95(3)	− 42.74(3)	2.89(3)	− 42.62(2)	2.22(3)	− 42.88(4)	300.9672	+1.1428
151	1.38(4)	− 42.55(3)	1.88(3)	− 42.69(3)	2.68(3)	− 42.59(2)	2.24(3)	− 42.73(3)	300.9672	+1.1409
153	1.74(4)	− 42.59(3)	2.56(3)	− 42.84(2)	4.04(3)	− 42.77(1)	2.78(3)	− 43.02(3)	300.9672	+1.1459
154	1.59(3)	− 42.46(2)	2.32(3)	− 42.68(2)	3.62(3)	− 42.71(1)	2.44(3)	− 42.80(2)	300.9647	+1.1440
155	1.82(3)	− 42.60(2)	2.35(3)	− 42.68(2)	3.23(3)	− 42.61(1)	2.76(3)	− 42.76(2)	300.9678	+1.1409
156	1.69(3)	− 42.64(2)	2.15(3)	− 42.69(2)	3.02(2)	− 42.61(1)	2.68(3)	− 42.79(2)	300.9691	+1.1409
157	2.01(3)	− 42.53(2)	2.74(2)	− 42.76(1)	4.05(2)	− 42.67(1)	2.99(3)	− 42.91(2)	300.9672	+1.1434
158	2.06(2)	− 42.55(2)	2.69(2)	− 42.69(1)	3.82(2)	− 42.63(1)	2.94(2)	− 42.87(2)	300.9678	+1.1421
159	2.05(3)	− 42.58(2)	2.63(2)	− 42.70(1)	3.84(2)	− 42.64(1)	2.93(3)	− 42.86(2)	300.9678	+1.1421
160	1.85(3)	− 42.51(2)	2.47(3)	− 42.71(2)	3.57(3)	− 42.60(1)	2.79(3)	− 42.82(3)	300.9666	+1.1415
162	1.94(3)	− 42.61(2)	2.34(3)	− 42.66(2)	3.30(2)	− 42.60(1)	2.69(3)	− 42.79(2)	300.9684	+1.1409
163	1.79(3)	− 42.57(2)	2.41(3)	− 42.71(2)	3.54(3)	− 42.64(1)	2.67(3)	− 42.84(3)	300.9678	+1.1421
164	2.02(3)	− 42.59(2)	2.52(3)	− 42.72(2)	3.70(3)	− 42.64(1)	2.86(3)	− 42.82(2)	300.9678	+1.1421
165	1.93(3)	− 42.54(2)	2.50(2)	− 42.70(2)	3.66(2)	− 42.61(1)	2.75(3)	− 42.84(2)	300.9672	+1.1415
166	1.41(3)	− 42.62(3)	1.91(3)	− 42.61(2)	2.66(3)	− 42.54(2)	2.29(3)	− 42.70(2)	300.9678	+1.1390
167	1.90(3)	− 42.55(2)	2.40(3)	− 42.69(2)	3.51(3)	− 42.61(1)	2.55(3)	− 42.82(3)	300.9678	+1.1415
168	1.90(3)	− 42.61(2)	2.34(3)	− 42.70(2)	3.26(3)	− 42.59(1)	2.64(3)	− 42.81(2)	300.9684	+1.1409
169	1.94(3)	− 42.59(2)	2.71(2)	− 42.75(2)	3.98(3)	− 42.69(1)	2.89(3)	− 42.91(3)	300.9678	+1.1434
170	1.99(3)	− 42.59(2)	2.80(2)	− 42.75(1)	3.98(3)	− 42.67(1)	2.96(3)	− 42.91(2)	300.9678	+1.1434
171	1.97(2)	− 42.56(2)	2.60(2)	− 42.72(1)	3.61(2)	− 42.62(1)	2.79(2)	− 42.81(2)	300.9672	+1.1421
172	1.65(3)	− 42.57(2)	2.24(2)	− 42.67(2)	3.08(2)	− 42.56(1)	2.52(3)	− 42.79(3)	300.9678	+1.1409
173	1.48(3)	− 42.52(2)	2.07(2)	− 42.68(2)	2.87(2)	− 42.55(2)	2.47(3)	− 42.79(3)	300.9666	+1.1409
174	1.69(3)	− 42.56(2)	2.26(2)	− 42.72(2)	3.25(2)	− 42.58(1)	2.51(2)	− 42.83(2)	300.9678	+1.1415
175	1.47(3)	− 42.51(2)	1.98(3)	− 42.63(2)	2.76(2)	− 42.54(2)	2.31(3)	− 42.77(3)	300.9659	+1.1403
176	1.64(3)	− 42.51(2)	2.33(2)	− 42.71(2)	3.34(2)	− 42.61(1)	2.60(3)	− 42.86(3)	300.9672	+1.1421
177	1.75(3)	− 42.52(2)	2.39(2)	− 42.73(2)	3.29(2)	− 42.62(1)	2.60(3)	− 42.82(3)	300.9666	+1.1421
178	1.59(2)	− 42.55(2)	2.18(2)	− 42.71(2)	3.04(2)	− 42.58(1)	2.48(3)	− 42.85(2)	300.9678	+1.1415
179	1.55(3)	− 42.52(2)	2.19(2)	− 42.66(2)	2.98(2)	− 42.58(1)	2.53(3)	− 42.77(3)	300.9666	+1.1409

Table A2. Continued

	Parameters of Gaussian fits to transitions[a]								Best-fit locations[b]	
	N_2H^+		HNC		HCO^+		HCN			
No.	$\langle a \rangle$ (K)	$\langle v \rangle$ (km s^{-1})	$\langle a \rangle$ (K)	$\langle v \rangle$ (km s^{-1})	$\langle a \rangle$ (K)	$\langle v \rangle$ (km s^{-1})	$\langle a \rangle$ (K)	$\langle v \rangle$ (km s^{-1})	l (deg)	b (deg)
180	1.61(3)	− 42.66(2)	2.18(2)	− 42.70(2)	2.94(2)	− 42.62(1)	2.55(3)	− 42.81(2)	300.9691	+1.1409
181	1.68(2)	− 42.55(2)	2.48(2)	− 42.82(2)	3.79(2)	− 42.72(1)	2.69(3)	− 42.97(2)	300.9672	+1.1446
182	1.84(3)	− 42.58(2)	2.34(2)	− 42.75(2)	3.49(2)	− 42.63(1)	2.69(3)	− 42.83(2)	300.9678	+1.1421
183	1.75(3)	− 42.58(2)	2.37(2)	− 42.76(2)	3.52(2)	− 42.64(1)	2.63(3)	− 42.86(3)	300.9678	+1.1428
184	1.45(3)	− 42.49(3)	1.96(2)	− 42.67(2)	2.96(2)	− 42.55(2)	2.43(3)	− 42.82(3)	300.9716	+1.1415
185	1.48(2)	− 42.61(2)	2.01(2)	− 42.69(2)	2.56(3)	− 42.56(3)	2.41(3)	− 42.80(2)	300.9684	+1.1409
186	1.85(3)	− 42.59(2)	2.24(2)	− 42.67(2)	3.20(2)	− 42.55(1)	2.55(3)	− 42.83(3)	300.9703	+1.1409
187	1.60(3)	− 42.61(2)	2.03(3)	− 42.69(2)	2.88(2)	− 42.55(2)	2.46(3)	− 42.75(2)	300.9703	+1.1403
189	1.74(6)	− 42.63(4)	2.00(5)	− 42.64(4)	3.00(5)	− 42.54(3)	2.53(5)	− 42.73(5)	300.9678	+1.1396
190	1.85(3)	− 42.55(2)	2.39(2)	− 42.71(2)	3.49(2)	− 42.63(1)	2.62(3)	− 42.83(3)	300.9672	+1.1421
191	1.71(2)	− 42.60(2)	2.22(2)	− 42.68(2)	3.12(2)	− 42.60(1)	2.49(2)	− 42.76(2)	300.9678	+1.1409
192	1.79(3)	− 42.64(2)	2.20(3)	− 42.68(2)	2.99(3)	− 42.59(2)	2.53(3)	− 42.72(2)	300.9684	+1.1396
193	2.00(3)	− 42.59(2)	2.37(3)	− 42.70(2)	3.34(3)	− 42.61(2)	2.73(3)	− 42.79(2)	300.9678	+1.1415
194	1.98(2)	− 42.61(2)	2.44(2)	− 42.69(1)	3.50(2)	− 42.63(1)	2.67(3)	− 42.76(2)	300.9684	+1.1409
196	1.88(3)	− 42.57(2)	2.45(2)	− 42.73(2)	3.64(2)	− 42.64(1)	2.74(3)	− 42.88(2)	300.9678	+1.1428
197	1.60(3)	− 42.58(2)	2.13(2)	− 42.66(2)	3.11(2)	− 42.60(1)	2.53(3)	− 42.78(2)	300.9678	+1.1409
198	1.74(3)	− 42.58(2)	2.25(2)	− 42.70(2)	3.19(2)	− 42.58(1)	2.56(3)	− 42.77(2)	300.9678	+1.1409
199	1.81(3)	− 42.56(2)	2.39(3)	− 42.73(2)	3.59(3)	− 42.64(1)	2.60(3)	− 42.82(3)	300.9672	+1.1421
200	1.86(3)	− 42.58(2)	2.37(2)	− 42.70(2)	3.49(2)	− 42.62(1)	2.66(3)	− 42.82(2)	300.9678	+1.1415
201	1.83(3)	− 42.59(2)	2.31(2)	− 42.71(2)	3.24(2)	− 42.62(1)	2.70(3)	− 42.78(2)	300.9678	+1.1409
202	1.78(2)	− 42.61(2)	2.38(2)	− 42.73(1)	3.32(2)	− 42.61(1)	2.69(3)	− 42.83(2)	300.9691	+1.1415
203	1.26(2)	− 42.45(3)	2.14(2)	− 42.76(2)	3.34(2)	− 42.64(1)	2.49(3)	− 42.99(3)	300.9716	+1.1453
204	1.64(3)	− 42.57(2)	2.14(2)	− 42.75(2)	3.17(2)	− 42.63(1)	2.46(3)	− 42.87(2)	300.9678	+1.1428
208	1.66(3)	− 42.59(2)	2.11(3)	− 42.73(2)	2.97(2)	− 42.59(1)	2.52(3)	− 42.77(2)	300.9684	+1.1409
209	1.85(3)	− 42.58(2)	2.47(3)	− 42.75(2)	3.75(3)	− 42.70(1)	2.61(3)	− 42.89(3)	300.9672	+1.1434
210	1.72(3)	− 42.61(2)	2.27(3)	− 42.70(2)	3.31(2)	− 42.64(1)	2.59(3)	− 42.83(2)	300.9684	+1.1415
211	1.70(3)	− 42.56(2)	2.03(2)	− 42.67(2)	2.74(2)	− 42.62(2)	2.15(3)	− 42.86(3)	300.9678	+1.1415
212	1.60(3)	− 42.64(2)	2.01(2)	− 42.69(2)	2.98(2)	− 42.60(1)	2.53(2)	− 42.78(2)	300.9684	+1.1409
213	1.56(3)	− 42.59(2)	2.12(2)	− 42.71(2)	2.99(2)	− 42.58(1)	2.49(3)	− 42.76(2)	300.9678	+1.1409
214	1.73(3)	− 42.59(2)	2.39(3)	− 42.71(2)	3.35(3)	− 42.64(1)	2.58(3)	− 42.83(3)	300.9678	+1.1421
215	1.47(2)	− 42.55(2)	2.10(2)	− 42.79(2)	3.24(2)	− 42.67(1)	2.46(2)	− 42.88(2)	300.9666	+1.1434
216	1.45(4)	− 42.58(3)	1.92(3)	− 42.72(3)	2.82(3)	− 42.56(2)	2.30(4)	− 42.72(4)	300.9678	+1.1403
218	1.45(3)	− 42.58(3)	1.95(3)	− 42.68(2)	2.70(3)	− 42.59(2)	2.30(3)	− 42.80(3)	300.9678	+1.1415
219	1.56(3)	− 42.58(2)	2.17(2)	− 42.71(2)	3.31(2)	− 42.64(1)	2.47(3)	− 42.87(3)	300.9684	+1.1421
220	1.76(3)	− 42.58(2)	2.23(3)	− 42.69(2)	3.45(3)	− 42.65(1)	2.51(3)	− 42.82(3)	300.9678	+1.1421
221	1.82(4)	− 42.58(3)	2.31(3)	− 42.71(2)	3.37(3)	− 42.64(2)	2.55(3)	− 42.84(3)	300.9678	+1.1421
222	1.19(2)	− 42.52(3)	1.85(2)	− 42.64(2)	2.73(2)	− 42.60(2)	2.22(3)	− 42.90(3)	300.9703	+1.1421
224	1.86(2)	− 42.56(2)	2.40(2)	− 42.70(1)	3.42(2)	− 42.61(1)	2.66(2)	− 42.83(2)	300.9678	+1.1415
225	1.40(3)	− 42.53(2)	2.08(2)	− 42.79(2)	3.27(2)	− 42.68(1)	2.38(3)	− 42.99(3)	300.9678	+1.1440
226	1.44(3)	− 42.61(2)	2.08(2)	− 42.75(2)	3.19(2)	− 42.65(1)	2.39(3)	− 42.88(3)	300.9684	+1.1428
228	1.27(3)	− 42.61(3)	1.74(2)	− 42.65(2)	2.52(2)	− 42.57(2)	2.12(3)	− 42.81(3)	300.9697	+1.1409
229	1.49(3)	− 42.58(3)	1.96(3)	− 42.73(2)	2.76(3)	− 42.58(2)	2.29(3)	− 42.77(3)	300.9678	+1.1409
230	1.53(3)	− 42.57(2)	1.97(3)	− 42.72(2)	2.83(3)	− 42.64(2)	2.29(3)	− 42.80(3)	300.9672	+1.1421
231	1.71(2)	− 42.57(2)	2.25(2)	− 42.70(2)	3.34(2)	− 42.63(1)	2.49(2)	− 42.84(2)	300.9678	+1.1421
232	1.37(3)	− 42.55(3)	1.89(2)	− 42.73(2)	2.89(2)	− 42.63(1)	2.25(3)	− 42.84(3)	300.9678	+1.1421
233	1.52(3)	− 42.58(3)	1.90(3)	− 42.68(2)	2.79(3)	− 42.60(2)	2.28(3)	− 42.83(3)	300.9678	+1.1415
234	1.24(3)	− 42.45(3)	1.86(2)	− 42.68(2)	2.81(2)	− 42.60(2)	2.25(3)	− 42.83(3)	300.9659	+1.1421
236	1.62(3)	− 42.54(2)	2.28(2)	− 42.76(2)	3.25(2)	− 42.65(1)	2.50(3)	− 42.91(3)	300.9678	+1.1434
237	1.63(3)	− 42.57(2)	2.21(3)	− 42.73(2)	3.31(3)	− 42.63(1)	2.39(3)	− 42.84(3)	300.9678	+1.1421
238	1.52(3)	− 42.58(2)	1.93(3)	− 42.69(2)	2.79(3)	− 42.57(2)	2.33(3)	− 42.71(3)	300.9672	+1.1403
239	1.49(3)	− 42.64(3)	1.94(3)	− 42.70(2)	2.85(3)	− 42.61(2)	2.24(3)	− 42.81(3)	300.9691	+1.1409
240	1.62(3)	− 42.59(2)	2.16(2)	− 42.73(2)	3.01(2)	− 42.62(1)	2.42(3)	− 42.79(2)	300.9678	+1.1415
241	1.77(4)	− 42.60(3)	2.33(3)	− 42.69(2)	3.09(3)	− 42.63(2)	2.61(4)	− 42.74(3)	300.9678	+1.1409
242	1.54(2)	− 42.57(2)	2.05(2)	− 42.69(2)	3.15(2)	− 42.62(1)	2.41(3)	− 42.83(2)	300.9678	+1.1415
243	1.03(4)	− 42.55(4)	1.93(3)	− 42.84(3)	3.17(3)	− 42.74(2)	2.32(4)	− 43.14(4)	300.9691	+1.1459
245	1.09(3)	− 42.53(4)	1.57(3)	− 42.64(3)	2.32(3)	− 42.56(2)	1.83(3)	− 42.75(4)	300.9659	+1.1409

[a]Uncertainties are displayed in parentheses as 1σ uncertainties on the final digit.
[b]Best-fit locations are given assuming that the map taken on 2012 June 29 is correctly pointed.